

## Research



**Cite this article:** Girelli A, Giancesio G, Musesti A, Penta R. 2023 Effective governing equations for dual porosity Darcy–Brinkman systems subjected to inhomogeneous body forces and their application to the lymph node. *Proc. R. Soc. A* **479**: 20230137. <https://doi.org/10.1098/rspa.2023.0137>

Received: 21 February 2023

Accepted: 4 July 2023

**Subject Areas:**

applied mathematics, differential equations, mathematical modelling

**Keywords:**

homogenization, Darcy–Brinkman, lymph node

**Author for correspondence:**

R. Penta

e-mail: [raimondo.penta@glasgow.ac.uk](mailto:raimondo.penta@glasgow.ac.uk)

Electronic supplementary material is available online at <https://doi.org/10.6084/m9.figshare.c.6751500>.

# Effective governing equations for dual porosity Darcy–Brinkman systems subjected to inhomogeneous body forces and their application to the lymph node

A. Girelli<sup>1</sup>, G. Giancesio<sup>1,2</sup>, A. Musesti<sup>1</sup> and R. Penta<sup>3</sup>

<sup>1</sup>Dipartimento di Matematica e Fisica ‘N. Tartaglia’, Università Cattolica del Sacro Cuore, Brescia, Italy

<sup>2</sup>Mathematics for Technology, Medicine and Biosciences, Università degli Studi di Ferrara, Italy

<sup>3</sup>School of Mathematics and Statistics, University of Glasgow, Glasgow, UK

RP, 0000-0003-1202-8775

We derive the homogenized governing equations for a double porosity system where the fluid flow within the individual compartments is governed by the coupling between the Darcy and the Darcy–Brinkman equations at the *microscale*, and are subjected to inhomogeneous body forces. The homogenized *macroscale* results are obtained by means of the asymptotic homogenization technique and read as a double Darcy differential model with mass exchange between phases. The role of the microstructure is encoded in the effective hydraulic conductivities which are obtained by solving periodic cell problems whose properties are illustrated and compared. We conclude by solving the new model by means of a semi-analytical approach under the assumption of azimuthal axisymmetry to model the movement of fluid within a lymph node.

## 1. Introduction

Flow of a Newtonian fluid inside a rigid porous matrix can be macroscopically described by Darcy’s Law.

The law was formulated by Henry Darcy based on the results of experiments on the flow of water through beds of sand [1], and can be rigorously derived by a large variety of upscaling methods such as mixture theory and asymptotic homogenization, see, e.g. [2] and [3,4], respectively. An alternative approach that describes the fluid flow of a Newtonian fluid inside a rigid porous matrix relies on the Darcy–Brinkman equation. The equation has been introduced by Brinkman adding the so-called *Brinkman* term, that is, an additional viscous term to the classical Darcy equation [5], represented by a Laplacian weighted by an effective viscosity  $\mu_e$ . This model has been used widely to analyse high-porosity porous media. In particular, the Darcy–Brinkman formulation allows us to specify the boundary conditions [6] and the interaction between a free-fluid region and a porous region [7], having a differential form similar to the Stokes' one. Despite its practical feedback, the Darcy–Brinkman equation is more complex and less straightforward to justify than Darcy's Law via upscaling method such as homogenization, see, e.g. [3,8,9], and is also computationally more demanding. Furthermore, the Darcy and Darcy–Brinkman equations possess very different differential structures.

In this article, we derive a new macroscale model which is obtained by upscaling a system of partial differential equations resulting from the coupling between Darcy's and Darcy–Brinkman's models. This means that, while we are considering the interactions between two porous media, pore-scale inhomogeneities are already 'smoothed out' from a geometrical viewpoint, and the upscaling process is performed by considering the interaction between the two phases at the mesoscale level. The two media are both considered intrinsically incompressible and subjected to inhomogeneous body forces, which can, for example, arise from the application of electromagnetic fields on e.g. magnetorheological fluids or electrolytes, see also [10]. We have also assumed that the two compartments are exchanging mass through their interface, which is modelled as a semi-permeable membrane. As a result, we obtain a double porosity macroscale model which is equipped with an effective source. This latter comprises contributions related to both the meso- and macroscale variations of the prescribed body forces mediated by the properties of the mesoscale structure, as well as mass exchange terms involving the pressure jumps between the two compartments at the macroscale.

The derivation of the macroscopic equations related to this problem is as general as possible, so the model is applicable to a large variety of scenarios of interest involving multiscale fluid flow in porous media. However, the chief motivation driving the present study is the application of the results to fluid flow within a lymph node. The lymph node is an essential component of the immune and lymphatic system, playing a critical role in safeguarding the body against infection and disease. It accomplishes this by harbouring lymphocytes, including B and T cells, which travel through the bloodstream and reside within the nodes. B cells are responsible for generating antibodies that specifically attach to antigens, thus initiating an immune response. When B cells are stimulated, they can transform into plasma cells, which secrete antibodies, or memory cells that provide defence in future encounters. Additionally, antigen-presenting cells, such as dendritic cells, capture and process antigens from various sources. These cells migrate to the lymph nodes, presenting the antigens to T cells to activate them and start the adaptive immune response [11,12]. These substances are transported inside the nodes (which are scattered throughout the lymphatic system) by the interstitial fluid, called *lymph* once inside the lymphatic system [12]. The main features of the lymph node from a mechanical point of view are the presence of a thin channel near the wall (*subcapsular sinus*, SCS) where the fluid can flow freely surrounding a porous core (*lymphoid compartment*, LC) that is the *parenchyma* of the lymph node [13], where the fluid can enter from the SCS through a conduit system network [14–16] formed by fibroblastic reticular cells (FRCs). We can see a reconstruction of this conduit system in figure 1. The lymph flow inside lymph nodes has various important functions, such as directing the distribution of macromolecules, enhancing ligand expression, aligning the extracellular matrix and facilitating cell migration [11]. Additionally, the fluid flow through the endothelial monolayers and fibroblastic reticular cell (FRC) network enhances the expression of chemokines, that generate a chemokine gradient by entering the lymph node, which helps in directing the localization and migration of immune cells [11,12]. Increased fluid flow also

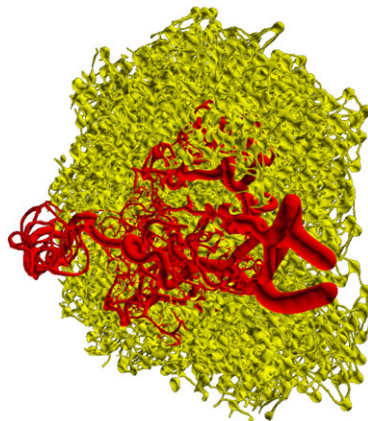


**Figure 1.** Reconstruction of the conduit system network (in yellow) and of the blood vessel network (in red) inside the lymphoid compartment. This figure is taken from [15] and reproduced with permission from Bocharov.

enhances the proliferation and drug sensitivity of certain types of lymphomas [17]. The study of fluid flow is significant in understanding tumour metastasis [18] and drug transport [19]. Furthermore, damage to or removal of lymph nodes can lead to lymphoedema [20,21], a condition related to inadequate lymph transport [20]. In particular, in this paper we focus our attention on the porous region of the lymph node (the LC) and the fluid exchange between the node and the blood vessels, which are only in this part of the node [22–24]; using the hypothesis of axisymmetry and isotropy of the porous medium, we find an explicit solution and analyse it by varying physiological parameters related to the lymph node.

As far as we know, the lymph flow through a lymph node has not been extensively explored from a mechanical and fluid dynamical perspective, and only a few models in the literature try to describe the behaviour of a lymph node (LN) from a fluid dynamical point of view [25,26]. In [27,28], they simulate the fluid flow inside the lymph node using an image-based modelling approach to investigate how the internal structure of the node affects the fluid flow pathways within the node. In [22], they developed a computational flow model based on the mouse popliteal LN, and they identify the important system characteristics by doing a parameter sensitivity analysis. In [15], they propose an object-oriented computational algorithm to model the three-dimensional geometry of the fibroblastic reticular cell graph network and the microvasculature, and then they analyse the lymph flow properties through the edges and the vertex of the conduit network. In [16], they developed a computational modelling algorithm that generates the conduit system graph network and then they study the fluid flow inside them imposing momentum balance along each segment and mass conservation in every node of the network. In [29], they developed a microfluidic platform replicating the lymph node microenvironment, they simulate the fluid flow in this microenvironment and then they visualize the direction of the fluid flow within the device using live imaging microscopy. Another microfluidic platform was developed by Birmingham *et al.* [18] that recreates the fluid dynamics of the lymph node's subcapsular sinus microenvironment; they estimate the levels of wall shear stress and evaluate how physiological flow patterns impact the adhesion of metastatic cancer cells. Tretiakova *et al.* [30] developed an artificial neural network model to describe the lymph node drainage function. The first attempts to describe the fluid flow in the lymph node from a more explicit point of view are in [31,32], where an explicit and a numerical solution are presented in a time-dependent setting in simplified geometries (a very idealized geometry for [31] and a spherical geometry in [32]), without considering the drainage of the blood vessels. The model presented in this work allows us to describe the blood vessel's drainage function in the lymph node considering the multiscale nature of the latter, obtaining a rigorous mathematical model

using the asymptotic homogenization technique that describes the fluid flow inside both the FRC and the blood vessels networks. Moreover, thanks to the fact that we start with a formulation that is already smoothed out, we do not need precise information about the microstructure geometry of the lymph node, which is in general very complex and hard to describe.

The work is organized as follows. In §2, we define the starting equations of our problem. We formulate the balance equations of Continuum Mechanics and the corresponding boundary conditions. In §3, we use the asymptotic homogenization technique to find the equations that describe the motion of the fluid at the macroscale, one starting with the Darcy–Brinkman equation and the other with the Darcy equation, and to describe the fluid exchange between them. In §4, we find the macroscopic equations by averaging the leading order terms of the asymptotic expansion. In §5, we analyse the difference in having as a microscale cell problem Darcy, Darcy–Brinkman or Stokes, finding an explicit result to the microscale cell problem in a specific case. In §6, we find the macroscopic explicit solution in a sphere with axisymmetry and isotropic permeability in terms of Bessel’s and Legendre’s polynomials. Finally, in §7, we analyse the solution found in §6 with lymph node physiological data obtained from the literature.

## 2. Statement of the problem

Let us consider a domain  $\Omega = \Omega_v \cup \Omega_m$ , where  $\Omega_m$  and  $\Omega_v$  are the portions of the domain that indicate two different phases. The labels  $m$  and  $v$  stand for the *matrix* and the *vessel* regions, respectively.

We use Darcy equation with inhomogeneous body forces to describe the fluid flow in the domain  $\Omega_v$  [10]:

$$\left. \begin{aligned} \mathbf{u}_v(\mathbf{x}) &= -\hat{\mathbf{K}}_v(\mathbf{x})(\nabla p_v(\mathbf{x}) - \mathbf{f}_v(\mathbf{x})) && \text{in } \Omega_v \\ \nabla \cdot \mathbf{u}_v(\mathbf{x}) &= 0 && \text{in } \Omega_v. \end{aligned} \right\} \quad (2.1)$$

The Darcy–Brinkman equation with inhomogeneous body forces in the phase  $\Omega_m$  can be written as

$$\left. \begin{aligned} -\nabla p_m(\mathbf{x}) - \hat{\mathbf{K}}_m^{-1}(\mathbf{x})\mathbf{u}_m(\mathbf{x}) + \mu_e \Delta \mathbf{u}_m(\mathbf{x}) + \mathbf{f}_m(\mathbf{x}) &= \mathbf{0} && \text{in } \Omega_m \\ \nabla \cdot \mathbf{u}_m(\mathbf{x}) &= 0 && \text{in } \Omega_m. \end{aligned} \right\} \quad (2.2)$$

Here we are considering two fluid phases: one in  $\Omega_v$  and one in  $\Omega_m$ . For  $\gamma = v, m$ ,  $\mathbf{u}_\gamma$  is the velocity of the fluid,  $p_\gamma$  the pressure,  $\mathbf{f}_\gamma$  the external force density,  $\hat{\mathbf{K}}_\gamma(\mathbf{x})$  is *hydraulic conductivity tensor*, which is given by the permeability tensor divided by the viscosity  $\mu$  of the fluid, and  $\mu_e$  is the *effective viscosity*. We assume that the hydraulic conductivity tensor is symmetric and positive definite, that is

$$\hat{\mathbf{K}}_\gamma(\mathbf{x}) = \hat{\mathbf{K}}_\gamma^T(\mathbf{x}), \quad \forall \mathbf{a} \neq \mathbf{0} : \mathbf{a} \cdot \hat{\mathbf{K}}_\gamma(\mathbf{x}) \cdot \mathbf{a} > 0.$$

As our starting points are the Darcy and Darcy–Brinkman representations, the pore structure is considered already smoothed out, and the microscale geometry information is encoded in the hydraulic conductivity  $\hat{\mathbf{K}}_\gamma(\mathbf{x})$ .

The interface conditions are prescribed as follows:

$$\left. \begin{aligned} \mathbf{u}_v(\mathbf{x}) \cdot \mathbf{n} = \mathbf{u}_m(\mathbf{x}) \cdot \mathbf{n} = L_p(p_m(\mathbf{x}) - p_v(\mathbf{x}) - \bar{p}) &&& \text{on } \Gamma \\ \mathbf{u}_m(\mathbf{x}) \cdot \boldsymbol{\tau} = -\frac{\sqrt{\mu \hat{\mathbf{K}}_m(\mathbf{x})}}{\alpha} [(\mathbf{n} \cdot \nabla) \mathbf{u}_m(\mathbf{x})] \cdot \boldsymbol{\tau} &&& \text{on } \Gamma, \end{aligned} \right\} \quad (2.3)$$

where  $\Gamma = \partial\Omega_m \cap \partial\Omega_v$  is the interface between the domains  $\Omega_v$  and  $\Omega_m$ ,  $\mathbf{n}$  the outer normal to  $\Omega_m$ ,  $\boldsymbol{\tau}$  any tangential vector to  $\Gamma$ ,  $\bar{p}$  is a constant and  $\alpha$  is a constant that must be found with experiments. The second equation of (2.3) is the *Beavers–Joseph–Saffman boundary condition* [33], which is a quite general interface condition on the tangent component of the velocity; instead, for the normal component of the velocity, we impose the interface condition described by the first equation of (2.3). We impose this type of interface condition having in mind biological applications of this model (such as lymph nodes, tumours); indeed, if we have  $\bar{p} = \sigma(\pi_m - \pi_v)$ , we obtain the *Starling equation* [34,35], which describes the fluid exchange between two different phases separated by a membrane, where  $\sigma$  is the *Staverman’s reflection coefficient*,  $\pi_v$  the *oncotic*

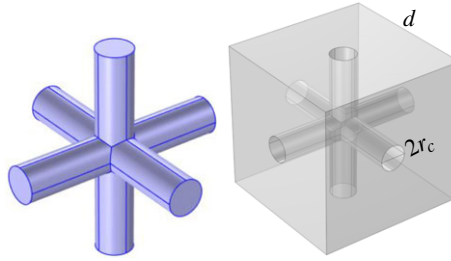


**Figure 2.** The cell problem domains  $\Omega_v$  (blue on the left) and  $\Omega_m$  (gray on the right), with the geometrical parameters in dimensional form, where  $r_c$  is the radius of the cylinders,  $d$  is the microscale variable, and  $\hat{r}_c = r_c/d$ .

pressure of phase  $\Omega_v$  and  $\pi_m$  the oncotic pressure of phase  $\Omega_m$ . For simplicity, in this work, we assume that the oncotic pressures  $\pi_v$  and  $\pi_m$  are constant, although in general, they can depend on the concentration of solutes which vary over time and space [36,37]. The quantity  $L_p$  is given by experimental measurements and depends on both the geometry and the tissue wall material of the intersection  $\Gamma$ . Nevertheless, our model remains valid for other choices of boundary conditions.

Now we want to write the Darcy–Brinkman equation and the interface conditions in a non-dimensional form; we define the following non-dimensional quantities (denoted with a prime symbol):

$$p = Pp', \quad \mathbf{u} = U\mathbf{u}', \quad \mathbf{x} = L\mathbf{x}' \quad \text{and} \quad \epsilon = \frac{d}{L},$$

where  $P$  is the characteristic pressure,  $U$  is the characteristic velocity,  $d$  is the fine scale length and  $L$  is the coarse scale length. In particular,  $d$  physically represents the distance between two vascularized regions. Here we are not resolving the fine details characterizing individual vessels and we instead represent the vascular network region as a domain  $\Omega_v$  geometrically consisting of interconnected cylinders (figure 2), where Darcy’s Law holds. As such,  $d$  is then identified as the distance between two such adjacent cylinders.  $C$  is a representative pressure gradient (with  $P = CL$ ), say:

$$C = \frac{U}{K_{\text{ref}}},$$

where  $K_{\text{ref}}$  is the representative (scalar) value for the hydraulic conductivity given by

$$K_{\text{ref}} \approx \frac{d^2}{\mu},$$

and we set

$$\mathbf{K}'_\gamma = \frac{\hat{\mathbf{K}}_\gamma}{K_{\text{ref}}} \quad \text{and} \quad f'_\gamma = \frac{f_\gamma}{C},$$

where  $\gamma = m, v$ . Substituting into (2.2) and omitting the primes, we obtain:

$$\left. \begin{aligned} -\nabla p_m(\mathbf{x}) - \mathbf{K}_m^{-1}(\mathbf{x})\mathbf{u}_m(\mathbf{x}) + \hat{\mu} \Delta \mathbf{u}_m(\mathbf{x}) + f_m(\mathbf{x}) &= \mathbf{0} & \text{in } \Omega_m, \\ \nabla \cdot \mathbf{u}_m(\mathbf{x}) &= 0 & \text{in } \Omega_m, \end{aligned} \right\} \quad (2.4)$$

where

$$\hat{\mu} = \frac{K_{\text{ref}}\mu_e}{L^2}.$$

Assuming that  $\mu_e \approx \mu$ , we have  $\hat{\mu} \approx O(\epsilon^2)$ .

Substituting these relations into (2.1) and (2.4), we obtain the non-dimensional equations:

$$\left. \begin{aligned} \mathbf{u}_v(\mathbf{x}) &= -\mathbf{K}_v(\mathbf{x})(\nabla p_v(\mathbf{x}) - \mathbf{f}_v(\mathbf{x})) && \text{in } \Omega_v \\ \nabla \cdot \mathbf{u}_v(\mathbf{x}) &= 0 && \text{in } \Omega_v, \end{aligned} \right\} \quad (2.5)$$

and

$$\left. \begin{aligned} -\nabla p_m(\mathbf{x}) - \mathbf{K}_m^{-1}(\mathbf{x})\mathbf{u}_m(\mathbf{x}) + \epsilon^2 \mu^* \Delta \mathbf{u}_m(\mathbf{x}) + \mathbf{f}_m(\mathbf{x}) &= \mathbf{0} && \text{in } \Omega_m, \\ \nabla \cdot \mathbf{u}_m(\mathbf{x}) &= 0 && \text{in } \Omega_m, \end{aligned} \right\} \quad (2.6)$$

where  $\mu^* = \mu_e/\mu$ .

Now we want to non-dimensionalize the interface conditions (2.3): by the Starling equation, the flux  $J_v$  passing through the interface between the two phases is given by

$$J_v = L_p \bar{S} (p_m(\mathbf{x}) - p_v(\mathbf{x}) - \bar{p}),$$

where  $\bar{S}$  is the total exchange surface density. From the fact that  $d$  is related to the distance between the vessels of the domain  $\Omega_v$ , we have

$$\bar{S} \propto \frac{L}{d} = \frac{1}{\epsilon}.$$

It is likely that the measured flux of a specific area of tissue will remain finite, even if the number of capillaries and their total surface area within that volume increases; hence we need to scale the interface condition by  $\epsilon$  to have a finite flux. The same conclusion can also be recovered for the Beavers–Joseph–Saffman interface condition (see [36] for more details).

Then, if we non-dimensionalize and we substitute the previous fact into equation (2.3) we have

$$\left. \begin{aligned} \mathbf{u}_v(\mathbf{x}) \cdot \mathbf{n} &= \mathbf{u}_m(\mathbf{x}) \cdot \mathbf{n} = \epsilon \bar{L}_p (p_m(\mathbf{x}) - p_v(\mathbf{x}) - \bar{p}) && \text{on } \Gamma \\ \mathbf{u}_m(\mathbf{x}) \cdot \boldsymbol{\tau} &= -\epsilon \frac{\sqrt{K_m(\mathbf{x})}}{\alpha} [(\mathbf{n} \cdot \nabla) \mathbf{u}_m(\mathbf{x})] \cdot \boldsymbol{\tau} && \text{on } \Gamma, \end{aligned} \right\} \quad (2.7)$$

where  $\bar{L}_p = L_p \mu L^2 / d^3$  [36].

### 3. Asymptotic homogenization

In this section, we employ the asymptotic homogenization technique [3,4] to derive a continuum macroscale model for the systems (2.5)–(2.7). Since we suppose  $\epsilon = (d/L) \ll 1$ , we enforce the sharp length-scale separation between  $d$  (fine scale) and  $L$  (coarse scale) and we decouple spatial scales by introducing a new local variable

$$\mathbf{y} = \frac{\mathbf{x}}{\epsilon}, \quad (3.1)$$

where  $\mathbf{x}$  and  $\mathbf{y}$  represent the coarse and fine scale spatial coordinates, respectively. They have to be formally considered independent variables. From now on,  $p_\gamma$ ,  $\mathbf{u}_\gamma$ ,  $\mathbf{K}_\gamma$  and  $\mathbf{f}_\gamma$  (where  $\gamma = m, v$ ) are assumed to depend on both  $\mathbf{x}$  and  $\mathbf{y}$ .

Before we start with the asymptotic homogenization technique, we recall some assumptions concerning the geometry of the multiscale problem:

- *Local periodicity*: we assume that  $p_\gamma$ ,  $\mathbf{u}_\gamma$ ,  $\mathbf{K}_\gamma$  and  $\mathbf{f}_\gamma$  are  $\mathbf{y}$ -periodic. This assumption allows us to study fine scale variations of the fields on a restricted portion of the domain. In particular, we have that  $\Omega$  is the periodic cell domain, and  $\Omega_m$  and  $\Omega_v$  are the portions of the domain  $\Omega$  related to the two different phases.
- *Macroscopic uniformity*: we neglect geometric variations of the cell and inclusions with respect to the coarse scale variable  $\mathbf{x}$ . Thanks to this assumption, we can consider only one periodic cell  $\Omega_\gamma$  for every macroscale point  $\mathbf{x}$ , and we have that

$$\nabla_{\mathbf{x}} \cdot \int_{\Omega_\gamma} (\cdot) \, d\mathbf{y} = \int_{\Omega_\gamma} \nabla_{\mathbf{x}} \cdot (\cdot) \, d\mathbf{y}. \quad (3.2)$$

The differential operator transforms accordingly

$$\nabla \rightarrow \nabla_x + \frac{1}{\epsilon} \nabla_y. \quad (3.3)$$

Now we employ a power series representation with respect to  $\epsilon$  as follows (with  $\gamma = m, v$ ):

$$\mathbf{u}_\gamma(x, \mathbf{y}) \equiv \mathbf{u}_\gamma^\epsilon(x, \mathbf{y}) = \sum_{l=0}^{\infty} \mathbf{u}_\gamma^{(l)}(x, \mathbf{y}) \epsilon^l, \quad (3.4)$$

$$p_\gamma(x, \mathbf{y}) \equiv p_\gamma^\epsilon(x, \mathbf{y}) = \sum_{l=0}^{\infty} p_\gamma^{(l)}(x, \mathbf{y}) \epsilon^l, \quad (3.5)$$

and

$$\mathbf{f}_\gamma(x, \mathbf{y}) \equiv \mathbf{f}_\gamma^\epsilon(x, \mathbf{y}) = \sum_{l=0}^{\infty} \mathbf{f}_\gamma^{(l)}(x, \mathbf{y}) \epsilon^l. \quad (3.6)$$

Substituting the power series representations (3.4)–(3.6) and the differential operator (3.3) into the non-dimensionalized Darcy equation (2.5), the Darcy–Brinkman equation (2.6) and the interface conditions (2.7), we have:

$$\left. \begin{aligned} \epsilon \mathbf{u}_v^\epsilon(x, \mathbf{y}) + \epsilon \mathbf{K}_v(x, \mathbf{y}) \nabla_x p_v^\epsilon(x, \mathbf{y}) \\ + \mathbf{K}_v(x, \mathbf{y}) \nabla_y p_v^\epsilon(x, \mathbf{y}) - \epsilon \mathbf{K}_v(x, \mathbf{y}) \mathbf{f}_v^\epsilon(x, \mathbf{y}) = \mathbf{0} \quad \text{in } \Omega_v, \\ \epsilon \nabla_x \cdot \mathbf{u}_v^\epsilon(x, \mathbf{y}) + \nabla_y \cdot \mathbf{u}_v^\epsilon(x, \mathbf{y}) = 0 \quad \text{in } \Omega_v, \end{aligned} \right\} \quad (3.7)$$

$$\left. \begin{aligned} -\epsilon \nabla_x p_m^\epsilon(x, \mathbf{y}) - \nabla_y p_m^\epsilon(x, \mathbf{y}) - \epsilon \mathbf{K}_m^{-1}(x, \mathbf{y}) \mathbf{u}_m^\epsilon(x, \mathbf{y}) \\ + \mu^* \epsilon^3 \Delta_x \mathbf{u}_m^\epsilon(x, \mathbf{y}) + \mu^* \epsilon \Delta_y \mathbf{u}_m^\epsilon(x, \mathbf{y}) + \mu^* \epsilon^2 \nabla_x \cdot (\nabla_y \mathbf{u}_m^\epsilon(x, \mathbf{y})) \\ + \mu^* \epsilon^2 \nabla_y \cdot (\nabla_x \mathbf{u}_m^\epsilon(x, \mathbf{y})) + \epsilon \mathbf{f}_m^\epsilon(x, \mathbf{y}) = \mathbf{0}, \\ \epsilon \nabla_x \cdot \mathbf{u}_m^\epsilon(x, \mathbf{y}) + \nabla_y \cdot \mathbf{u}_m^\epsilon(x, \mathbf{y}) = 0 \end{aligned} \right\} \begin{array}{l} \text{in } \Omega_m \\ \text{in } \Omega_m, \end{array} \quad (3.8)$$

$$\left. \begin{aligned} \mathbf{u}_v^\epsilon(x, \mathbf{y}) \cdot \mathbf{n} = \mathbf{u}_m^\epsilon(x, \mathbf{y}) \cdot \mathbf{n} = \epsilon \bar{L}_p(p_m^\epsilon(x, \mathbf{y}) - p_v^\epsilon(x, \mathbf{y}) - \bar{p}) \quad \text{on } \Gamma \\ \mathbf{u}_m^\epsilon(x, \mathbf{y}) \cdot \boldsymbol{\tau} = -\epsilon \frac{\sqrt{\mathbf{K}_m(x, \mathbf{y})}}{\alpha} \left[ \left( \mathbf{n} \cdot \left( \nabla_x + \frac{1}{\epsilon} \nabla_y \right) \right) \mathbf{u}_m^\epsilon(x, \mathbf{y}) \right] \cdot \boldsymbol{\tau} \quad \text{on } \Gamma. \end{aligned} \right\} \quad (3.9)$$

If we collect the terms of order  $\epsilon^0$  in systems (3.7) and (3.8):

$$\nabla_y p_v^{(0)}(x, \mathbf{y}) = \mathbf{0} \Rightarrow p_v^{(0)} = p_v^{(0)}(x), \quad (3.10)$$

$$\nabla_y p_m^{(0)}(x, \mathbf{y}) = \mathbf{0} \Rightarrow p_m^{(0)} = p_m^{(0)}(x), \quad (3.11)$$

$$\nabla_y \cdot \mathbf{u}_v^{(0)}(x, \mathbf{y}) = 0, \quad (3.12)$$

and

$$\nabla_y \cdot \mathbf{u}_m^{(0)}(x, \mathbf{y}) = 0, \quad (3.13)$$

and for the interface conditions (3.9):

$$\mathbf{u}_m^{(0)}(x, \mathbf{y}) \cdot \mathbf{n} = \mathbf{u}_v^{(0)}(x, \mathbf{y}) \cdot \mathbf{n} = 0 \quad \text{on } \Gamma \quad (3.14)$$

and

$$\mathbf{u}_m^{(0)}(x, \mathbf{y}) \cdot \boldsymbol{\tau} = -\frac{\sqrt{\mathbf{K}_m(x, \mathbf{y})}}{\alpha} [(\mathbf{n} \cdot \nabla_y) \mathbf{u}_m^{(0)}(x, \mathbf{y})] \cdot \boldsymbol{\tau} \quad \text{on } \Gamma. \quad (3.15)$$

Collecting the terms of order  $\epsilon^1$  in systems (3.7) and (3.8) and in the interface conditions (3.9), we obtain:

$$\begin{aligned} \mathbf{u}_v^{(0)}(\mathbf{x}, \mathbf{y}) + \mathbf{K}_v(\mathbf{x}, \mathbf{y})(\nabla_x p_v^{(0)}(\mathbf{x})) \\ + \nabla_y p_v^{(1)}(\mathbf{x}, \mathbf{y}) - \mathbf{f}_v^{(0)}(\mathbf{x}, \mathbf{y}) = \mathbf{0} \quad \text{in } \Omega_v, \end{aligned} \quad (3.16)$$

$$\nabla_x \cdot \mathbf{u}_v^{(0)}(\mathbf{x}, \mathbf{y}) + \nabla_y \cdot \mathbf{u}_v^{(1)}(\mathbf{x}, \mathbf{y}) = 0 \quad \text{in } \Omega_v, \quad (3.17)$$

$$\begin{aligned} -\nabla_x p_m^{(0)}(\mathbf{x}) - \nabla_y p_m^{(1)}(\mathbf{x}, \mathbf{y}) - \mathbf{K}_m^{-1}(\mathbf{x}, \mathbf{y}) \mathbf{u}_m^{(0)}(\mathbf{x}, \mathbf{y}) \\ + \mu^* \Delta_y \mathbf{u}_m^{(0)}(\mathbf{x}, \mathbf{y}) + \mathbf{f}_m^{(0)}(\mathbf{x}, \mathbf{y}) = \mathbf{0} \quad \text{in } \Omega_m, \end{aligned} \quad (3.18)$$

$$\nabla_x \cdot \mathbf{u}_m^{(0)}(\mathbf{x}, \mathbf{y}) + \nabla_y \cdot \mathbf{u}_m^{(1)}(\mathbf{x}, \mathbf{y}) = 0 \quad \text{on } \Omega_m, \quad (3.19)$$

$$\mathbf{u}_m^{(1)}(\mathbf{x}, \mathbf{y}) \cdot \mathbf{n} = \mathbf{u}_v^{(1)}(\mathbf{x}, \mathbf{y}) \cdot \mathbf{n} = \bar{L}_p(p_m^{(0)}(\mathbf{x}) - p_v^{(0)}(\mathbf{x}) - \bar{p}) \quad \text{on } \Gamma \quad (3.20)$$

and

$$\begin{aligned} \mathbf{u}_m^{(1)}(\mathbf{x}, \mathbf{y}) \cdot \boldsymbol{\tau} = -\frac{\sqrt{\mathbf{K}_m(\mathbf{x}, \mathbf{y})}}{\alpha} [(\mathbf{n} \cdot \nabla_x) \mathbf{u}_m^{(0)}(\mathbf{x}, \mathbf{y}) \\ + (\mathbf{n} \cdot \nabla_y) \mathbf{u}_m^{(1)}(\mathbf{x}, \mathbf{y})] \cdot \boldsymbol{\tau} \quad \text{on } \Gamma. \end{aligned} \quad (3.21)$$

Applying the  $\nabla_y \cdot$  operator to equation (3.16) and using equation (3.12), we obtain

$$\nabla_y \cdot [\mathbf{K}_v(\mathbf{x}, \mathbf{y})(\nabla_x p_v^{(0)}(\mathbf{x}) + \nabla_y p_v^{(1)}(\mathbf{x}, \mathbf{y}) - \mathbf{f}_v^{(0)}(\mathbf{x}, \mathbf{y}))] = 0 \quad \text{in } \Omega_v, \quad (3.22)$$

and the boundary condition (3.14) becomes

$$[\mathbf{K}_v(\mathbf{x}, \mathbf{y})(\nabla_x p_v^{(0)}(\mathbf{x}) + \nabla_y p_v^{(1)}(\mathbf{x}, \mathbf{y}) - \mathbf{f}_v^{(0)}(\mathbf{x}, \mathbf{y}))] \cdot \mathbf{n} = 0 \quad \text{on } \Gamma. \quad (3.23)$$

Since the problem is linear and the vector function  $\nabla_x p^{(0)}$  is  $\mathbf{y}$ -constant, we state the following ansatz of the solution:

$$p_v^{(1)}(\mathbf{x}, \mathbf{y}) = \mathbf{g}_v(\mathbf{x}, \mathbf{y}) \cdot \nabla_x p_v^{(0)}(\mathbf{x}) + \tilde{g}_v(\mathbf{x}, \mathbf{y}). \quad (3.24)$$

Equation (3.24) is a solution of the problem (3.22) and (3.23) (up to a  $\mathbf{y}$ -constant function), provided that the auxiliary vector field  $\mathbf{g}_v$  and the auxiliary scalar function  $\tilde{g}_v$  solve the following cell problems:

$$\left. \begin{aligned} \nabla_y \cdot [\nabla_y \mathbf{g}_v(\mathbf{x}, \mathbf{y}) \mathbf{K}_v(\mathbf{x}, \mathbf{y})^T] &= -\nabla_y \cdot \mathbf{K}_v(\mathbf{x}, \mathbf{y})^T, \quad \text{in } \Omega_v \\ [\nabla_y \mathbf{g}_v(\mathbf{x}, \mathbf{y}) \mathbf{K}_v(\mathbf{x}, \mathbf{y})^T] \cdot \mathbf{n} &= -\mathbf{K}_v(\mathbf{x}, \mathbf{y})^T \cdot \mathbf{n} \quad \text{on } \Gamma, \end{aligned} \right\} \quad (3.25)$$

and

$$\left. \begin{aligned} \nabla_y \cdot [\mathbf{K}_v(\mathbf{x}, \mathbf{y}) \nabla_y \tilde{g}_v(\mathbf{x}, \mathbf{y})] &= \nabla_y \cdot \mathbf{K}_v(\mathbf{x}, \mathbf{y}) \mathbf{f}_v^{(0)}(\mathbf{x}, \mathbf{y}), \quad \text{in } \Omega_v \\ [\mathbf{K}_v(\mathbf{x}, \mathbf{y}) \nabla_y \tilde{g}_v(\mathbf{x}, \mathbf{y})] \cdot \mathbf{n} &= \mathbf{K}_v(\mathbf{x}, \mathbf{y}) \mathbf{f}_v^{(0)}(\mathbf{x}, \mathbf{y}) \cdot \mathbf{n} \quad \text{on } \Gamma. \end{aligned} \right\} \quad (3.26)$$

Moreover, we impose that  $\langle \mathbf{g}_v(\mathbf{x}, \mathbf{y}) \rangle_{\Omega_v} = 0$  and  $\langle \tilde{g}_v(\mathbf{x}, \mathbf{y}) \rangle_{\Omega_v} = 0$  to ensure the uniqueness of the solution, where  $\langle \cdot \rangle_{\Omega_v}$  is defined as

$$\langle h \rangle_{\Omega_v} = \frac{1}{|\Omega_v|} \int_{\Omega_v} h \, d\mathbf{y}. \quad (3.27)$$

To solve the Darcy–Brinkman problem in  $\Omega_m$ , since the problem is linear and the vector function  $\nabla_x p^{(0)}$  is  $\mathbf{y}$ -constant, we formulate the following ansatz for the solution:

$$p_m^{(1)}(\mathbf{x}, \mathbf{y}) = -\mathbf{g}_m(\mathbf{x}, \mathbf{y}) \cdot \nabla_x p_m^{(0)}(\mathbf{x}) + \tilde{g}_m(\mathbf{x}, \mathbf{y}) \quad (3.28)$$

and

$$\mathbf{u}_m^{(0)}(\mathbf{x}, \mathbf{y}) = -\mathbf{W}_m(\mathbf{x}, \mathbf{y}) \nabla_x p_m^{(0)}(\mathbf{x}) + \tilde{\mathbf{w}}_m(\mathbf{x}, \mathbf{y}). \quad (3.29)$$

Putting together equations (3.13)–(3.15) and (3.18), we obtain an auxiliary Darcy–Brinkman system in  $(\mathbf{u}_m^{(0)}, p_m^{(1)})$ . Hence, we have that (3.28) and (3.29) are solutions of the problem (3.13)–



(3.15) and (3.18) provided that the auxiliary fields  $\mathbf{g}_m$ ,  $\mathbf{W}_m$ ,  $\tilde{\mathbf{w}}_m$ , and  $\tilde{\mathbf{g}}_m$  solve the following cell problems:

$$\left. \begin{aligned} \mathbf{K}_m^{-1}(\mathbf{x}, \mathbf{y})\mathbf{W}_m(\mathbf{x}, \mathbf{y}) - \mu^* \Delta_{\mathbf{y}} \mathbf{W}_m(\mathbf{x}, \mathbf{y}) - \mathbb{I} \\ + (\nabla_{\mathbf{y}} \mathbf{g}_m(\mathbf{x}, \mathbf{y}))^T = \mathbf{0} & \quad \text{in } \Omega_m, \\ \nabla_{\mathbf{y}} \cdot \mathbf{W}_m(\mathbf{x}, \mathbf{y}) = \mathbf{0} & \quad \text{in } \Omega_m, \\ \mathbf{W}_m(\mathbf{x}, \mathbf{y}) \cdot \mathbf{n} = \mathbf{0} & \quad \text{on } \Gamma, \\ \mathbf{W}_m(\mathbf{x}, \mathbf{y}) \boldsymbol{\tau} = -\frac{\sqrt{\mathbf{K}_m(\mathbf{x}, \mathbf{y})}}{\alpha} [(\nabla_{\mathbf{y}} \mathbf{W}_m(\mathbf{x}, \mathbf{y})) \mathbf{n}] \boldsymbol{\tau} & \quad \text{on } \Gamma, \end{aligned} \right\} \quad (3.30)$$

and

$$\left. \begin{aligned} -\mathbf{K}_m^{-1}(\mathbf{x}, \mathbf{y})\tilde{\mathbf{w}}_m(\mathbf{x}, \mathbf{y}) + \mu^* \Delta_{\mathbf{y}} \tilde{\mathbf{w}}_m(\mathbf{x}, \mathbf{y}) - \nabla_{\mathbf{y}} \tilde{\mathbf{g}}_m(\mathbf{x}, \mathbf{y}) \\ + \mathbf{f}_m^{(0)}(\mathbf{x}, \mathbf{y}) = \mathbf{0} & \quad \text{in } \Omega_m, \\ \nabla_{\mathbf{y}} \cdot \tilde{\mathbf{w}}_m(\mathbf{x}, \mathbf{y}) = \mathbf{0} & \quad \text{in } \Omega_m, \\ \tilde{\mathbf{w}}_m(\mathbf{x}, \mathbf{y}) \cdot \mathbf{n} = 0 & \quad \text{on } \Gamma, \\ \tilde{\mathbf{w}}_m(\mathbf{x}, \mathbf{y}) \cdot \boldsymbol{\tau} = -\frac{\sqrt{\mathbf{K}_m(\mathbf{x}, \mathbf{y})}}{\alpha} [(\nabla_{\mathbf{y}} \tilde{\mathbf{w}}_m(\mathbf{x}, \mathbf{y})) \mathbf{n}] \boldsymbol{\tau} & \quad \text{on } \Gamma. \end{aligned} \right\} \quad (3.31)$$

Moreover, we impose that  $\langle \mathbf{g}_m(\mathbf{x}, \mathbf{y}) \rangle_{\Omega_m} = \mathbf{0}$  and  $\langle \tilde{\mathbf{g}}_m(\mathbf{x}, \mathbf{y}) \rangle_{\Omega_m} = \mathbf{0}$  to ensure the uniqueness of the solution.

## 4. The macroscopic model

Applying the average operator  $\langle \cdot \rangle_{\Omega_m}$  to the ansatz (3.29), we obtain:

$$\langle \mathbf{u}_m^{(0)}(\mathbf{x}, \mathbf{y}) \rangle_{\Omega_m} = -\langle \mathbf{W}_m(\mathbf{x}, \mathbf{y}) \rangle_{\Omega_m} \nabla_{\mathbf{x}} p_m^{(0)}(\mathbf{x}) + \langle \tilde{\mathbf{w}}_m(\mathbf{x}, \mathbf{y}) \rangle_{\Omega_m}, \quad (4.1)$$

where  $\mathbf{W}_m$  and  $\tilde{\mathbf{w}}_m$  solve (3.30) and (3.31), respectively.

We recall the equation of order  $\epsilon^1$  for the divergence (3.19):

$$\nabla_{\mathbf{x}} \cdot \mathbf{u}_m^{(0)}(\mathbf{x}, \mathbf{y}) + \nabla_{\mathbf{y}} \cdot \mathbf{u}_m^{(1)}(\mathbf{x}, \mathbf{y}) = 0.$$

Applying the average operator, we obtain, using the macroscopic uniformity assumption (3.2):

$$\nabla_{\mathbf{x}} \cdot \langle \mathbf{u}_m^{(0)}(\mathbf{x}, \mathbf{y}) \rangle_{\Omega_m} + \langle \nabla_{\mathbf{y}} \cdot \mathbf{u}_m^{(1)}(\mathbf{x}, \mathbf{y}) \rangle_{\Omega_m} = 0.$$

Moreover, using the divergence theorem and the interface conditions (3.20):

$$\begin{aligned} \langle \nabla_{\mathbf{y}} \cdot \mathbf{u}_m^{(1)} \rangle_{\Omega_m} &= \frac{1}{|\Omega_m|} \int_{\Omega_m} \nabla_{\mathbf{y}} \cdot \mathbf{u}_m^{(1)}(\mathbf{x}, \mathbf{y}) \, d\mathbf{y} = \frac{1}{|\Omega_m|} \int_{\Gamma} \mathbf{u}_m^{(1)}(\mathbf{x}, \mathbf{y}) \cdot \mathbf{n} \, dS \\ &= \frac{\bar{L}_p S}{|\Omega_m|} [p_m^{(0)}(\mathbf{x}) - p_v^{(0)}(\mathbf{x}) - \bar{p}], \end{aligned} \quad (4.2)$$

where  $|\Omega_m|$  is the volume fraction of the cell phase  $m$  and  $S$  is the unit cell capillary walls surface; hence we have

$$\nabla_{\mathbf{x}} \cdot \langle \mathbf{u}_m^{(0)}(\mathbf{x}, \mathbf{y}) \rangle_{\Omega_m} = -\frac{\bar{L}_p S}{|\Omega_m|} [p_m^{(0)}(\mathbf{x}) - p_v^{(0)}(\mathbf{x}) - \bar{p}]. \quad (4.3)$$

For the Darcy problem, we apply the average operator to equation (3.16) and, substituting the ansatz (3.24), we obtain

$$\begin{aligned} \langle \mathbf{u}_v^{(0)}(\mathbf{x}, \mathbf{y}) \rangle_{\Omega_v} &= -\langle \mathbf{K}_v(\mathbf{x}, \mathbf{y}) + \mathbf{K}_v(\mathbf{x}, \mathbf{y})(\nabla_{\mathbf{y}} \mathbf{g}_v(\mathbf{x}, \mathbf{y}))^T \rangle_{\Omega_v} \nabla_{\mathbf{x}} p_v^{(0)}(\mathbf{x}) \\ &\quad - \langle \mathbf{K}_v(\mathbf{x}, \mathbf{y}) \nabla_{\mathbf{y}} \tilde{\mathbf{g}}_v(\mathbf{x}, \mathbf{y}) \rangle_{\Omega_v} + \langle \mathbf{K}_v(\mathbf{x}, \mathbf{y}) \mathbf{f}_v^{(0)}(\mathbf{x}, \mathbf{y}) \rangle_{\Omega_v}. \end{aligned} \quad (4.4)$$

Using the same technique, applying the average operator and the divergence theorem to equation (3.17), it follows that

$$\nabla_x \cdot \langle \mathbf{u}_v^{(0)}(\mathbf{x}, \mathbf{y}) \rangle_{\Omega_v} = \frac{\bar{L}_p S}{|\Omega_v|} [p_m^{(0)}(\mathbf{x}) - p_v^{(0)}(\mathbf{x}) - \bar{p}], \quad (4.5)$$

where we considered that  $\mathbf{n}_v = -\mathbf{n}$ .

We can write the total macroscale velocity  $\mathbf{u}_C$  as

$$\begin{aligned} \mathbf{u}_C &= |\Omega_m| \langle \mathbf{u}_m^{(0)}(\mathbf{x}, \mathbf{y}) \rangle_{\Omega_m} + |\Omega_v| \langle \mathbf{u}_v^{(0)}(\mathbf{x}, \mathbf{y}) \rangle_{\Omega_v} \\ &= -|\Omega_m| \langle \mathbf{W}_m(\mathbf{x}, \mathbf{y}) \rangle_{\Omega_m} \nabla_x p_m^{(0)}(\mathbf{x}) + |\Omega_m| \langle \tilde{\mathbf{w}}_m(\mathbf{x}, \mathbf{y}) \rangle_{\Omega_m} \\ &\quad - |\Omega_v| \langle \mathbf{K}_v(\mathbf{x}, \mathbf{y}) + \mathbf{K}_v(\mathbf{x}, \mathbf{y}) (\nabla_y \mathbf{g}_v(\mathbf{x}, \mathbf{y}))^T \rangle_{\Omega_v} \nabla_x p_v^{(0)}(\mathbf{x}) \\ &\quad - |\Omega_v| \langle \mathbf{K}_v(\mathbf{x}, \mathbf{y}) \nabla_y \tilde{\mathbf{g}}_v(\mathbf{x}, \mathbf{y}) \rangle_{\Omega_v} + |\Omega_v| \langle \mathbf{K}_v(\mathbf{x}, \mathbf{y}) \mathbf{f}_v^{(0)}(\mathbf{x}, \mathbf{y}) \rangle_{\Omega_v}. \end{aligned} \quad (4.6)$$

**Remark 4.1.** We notice that the fluid is macroscopically incompressible, as the macroscale divergence of the leading-order average fluid velocity (4.6) reduces to zero by means of (4.5) and (4.3). The two individual phases can have non-zero divergences due to the fluid exchange between compartments, as in [36,38].

Substituting (4.1) into equation (4.3) and (4.4) into equation (4.5), respectively, we obtain

$$\begin{aligned} &\nabla_x \cdot \left( \langle \mathbf{W}_m(\mathbf{x}, \mathbf{y}) \rangle_{\Omega_m} \nabla_x p_m^{(0)}(\mathbf{x}) \right) \\ &= \nabla_x \cdot \langle \tilde{\mathbf{w}}_m(\mathbf{x}, \mathbf{y}) \rangle_{\Omega_m} + \frac{\bar{L}_p S}{|\Omega_m|} [p_m^{(0)}(\mathbf{x}) - p_v^{(0)}(\mathbf{x}) - \bar{p}], \end{aligned} \quad (4.7)$$

and

$$\begin{aligned} &\nabla_x \cdot \left( \langle \mathbf{K}_v(\mathbf{x}, \mathbf{y}) + \mathbf{K}_v(\mathbf{x}, \mathbf{y}) (\nabla_y \mathbf{g}_v(\mathbf{x}, \mathbf{y}))^T \rangle_{\Omega_v} \nabla_x p_v^{(0)}(\mathbf{x}) \right) \\ &= -\nabla_x \cdot \langle \mathbf{K}_v(\mathbf{x}, \mathbf{y}) \nabla_y \tilde{\mathbf{g}}_v(\mathbf{x}, \mathbf{y}) \rangle_{\Omega_v} \\ &\quad + \nabla_x \cdot \langle \mathbf{K}_v(\mathbf{x}, \mathbf{y}) \mathbf{f}_v^{(0)}(\mathbf{x}, \mathbf{y}) \rangle_{\Omega_v} - \frac{\bar{L}_p S}{|\Omega_m|} [p_m^{(0)}(\mathbf{x}) - p_v^{(0)}(\mathbf{x}) - \bar{p}]. \end{aligned} \quad (4.8)$$

The equations (4.7) and (4.8) are the classical Darcy Law diffusion problem with additional terms related to the multiscale forces [10] and the fluid exchange between phases. We note that if the multiscale forces  $\mathbf{f}_m$  and  $\mathbf{f}_v$  are zero, the unique solutions  $\tilde{\mathbf{g}}_v(\mathbf{x}, \mathbf{y})$  and  $\tilde{\mathbf{w}}_m(\mathbf{x}, \mathbf{y})$  of the systems (3.25) and (3.30) are both zero. In this latter case, equations (4.7) and (4.8) reduce to the double Darcy's model with fluid exchange between phases as derived in [38] and subsequently solved and generalized in [36,39], respectively. However, even when ignoring the contributions related to the external volume loads, the final model that we have obtained differs from the one obtained in [38] due to the Darcy–Brinkman type cell problem which is to be solved to compute the hydraulic conductivity  $\langle \mathbf{W}_m \rangle_{\Omega_m}$  for the matrix compartment  $\Omega_m$ .

Equations (4.1) and (4.3)–(4.5) are in non-dimensional form. We have the following relations:

$$|\Omega_m| = \frac{|\Omega_m^{\text{tot}}|}{|\Omega|}, \quad |\Omega_v| = \frac{|\Omega_v^{\text{tot}}|}{|\Omega|} \quad \text{and} \quad S = \frac{S^{\text{tot}} d}{|\Omega|}, \quad (4.9)$$

where  $|\Omega|$  is the total volume of the lymph node,  $|\Omega_m^{\text{tot}}|$  is the total volume of the phase  $m$ ,  $|\Omega_v^{\text{tot}}|$  is the total volume of the phase  $v$ , and  $S^{\text{tot}}$  is the total vessel surface. Thanks to the above relations, we have that equations (4.1), (4.3)–(4.5) in the dimensional form are

$$\langle \mathbf{u}_m^{(0)}(\mathbf{x}, \mathbf{y}) \rangle_{\Omega_m} = -\frac{d^2}{\mu} \langle \mathbf{W}_m(\mathbf{x}, \mathbf{y}) \rangle_{\Omega_m} \nabla_x p_m^{(0)}(\mathbf{x}) + \frac{Cd^2}{\mu} \langle \tilde{\mathbf{w}}_m(\mathbf{x}, \mathbf{y}) \rangle_{\Omega_m}, \quad (4.10)$$

$$\nabla_x \cdot \langle \mathbf{u}_m^{(0)}(\mathbf{x}, \mathbf{y}) \rangle_{\Omega_m} = -\frac{L_p S^{\text{tot}}}{|\Omega_m^{\text{tot}}|} [p_m^{(0)}(\mathbf{x}) - p_v^{(0)}(\mathbf{x}) - \bar{p}]. \quad (4.11)$$

$$\begin{aligned} \langle \mathbf{u}_v^{(0)}(\mathbf{x}, \mathbf{y}) \rangle_{\Omega_v} &= -\frac{d^2}{\mu} \langle \mathbf{K}_v(\mathbf{x}, \mathbf{y}) + \mathbf{K}_v(\mathbf{x}, \mathbf{y})(\nabla_y \mathbf{g}_v(\mathbf{x}, \mathbf{y}))^T \rangle_{\Omega_v} \nabla_x p_v^{(0)}(\mathbf{x}) \\ &\quad - \frac{Cd^2}{\mu} \langle \mathbf{K}_v(\mathbf{x}, \mathbf{y}) \nabla_y \tilde{\mathbf{g}}_v(\mathbf{x}, \mathbf{y}) \rangle_{\Omega_v} + \frac{d^2}{\mu} \langle \mathbf{K}_v(\mathbf{x}, \mathbf{y}) \mathbf{f}_v^{(0)}(\mathbf{x}, \mathbf{y}) \rangle_{\Omega_v}. \end{aligned} \quad (4.12)$$

and

$$\nabla_x \cdot \langle \mathbf{u}_v^{(0)}(\mathbf{x}, \mathbf{y}) \rangle_{\Omega_v} = \frac{L_p S^{\text{tot}}}{|\Omega_v^{\text{tot}}|} [p_m^{(0)}(\mathbf{x}) - p_v^{(0)}(\mathbf{x}) - \bar{p}], \quad (4.13)$$

and then we call

$$\bar{\mathbf{K}}_m = \frac{d^2}{\mu} \langle \mathbf{W}_m(\mathbf{x}, \mathbf{y}) \rangle_{\Omega_m} \quad (4.14)$$

and

$$\bar{\mathbf{K}}_v = \frac{d^2}{\mu} \langle \mathbf{K}_v(\mathbf{x}, \mathbf{y}) + \mathbf{K}_v(\mathbf{x}, \mathbf{y})(\nabla_y \mathbf{g}_v(\mathbf{x}, \mathbf{y}))^T \rangle_{\Omega_v}, \quad (4.15)$$

the dimensional hydraulic conductivity of the phase  $m$  and  $v$ , respectively.

## 5. A comparison between different fluid regimes

In this section, we want to study the differences in using Darcy, Stokes or Darcy–Brinkman for the domain  $\Omega_v$  in the cell problem. We can see the cell problem domain in figure 2.

For simplicity, we focus on the case  $\mathbf{f}_v = \mathbf{0}$ , replacing the interface boundary conditions with the no-slip condition  $\mathbf{u}_v = \mathbf{0}$  and assuming the isotropy of the porous medium, that is  $\mathbf{K}_v = K_v \mathbb{I}$ . Hence the Darcy cell problems (3.25) and (3.26) reduce to

$$\left. \begin{aligned} \nabla_y \cdot [\nabla_y \mathbf{g}_v(\mathbf{x}, \mathbf{y})] &= 0, & \text{in } \Omega_v \\ \nabla_y \mathbf{g}_v(\mathbf{x}, \mathbf{y}) \cdot \mathbf{n} &= -\mathbf{n} & \text{on } \Gamma, \end{aligned} \right\} \quad (5.1)$$

while the Darcy–Brinkman cell problems (3.30) and (3.31) reduce to

$$\left. \begin{aligned} K^{*-1} \mathbf{W}_v^{\text{DB}}(\mathbf{x}, \mathbf{y}) - \mu^* \Delta_y \mathbf{W}_v^{\text{DB}}(\mathbf{x}, \mathbf{y}) - \mathbb{I} + (\nabla_y \mathbf{g}_v^{\text{DB}}(\mathbf{x}, \mathbf{y}))^T &= \mathbf{0} & \text{in } \Omega_v, \\ \nabla_y \cdot \mathbf{W}_v^{\text{DB}}(\mathbf{x}, \mathbf{y}) &= 0 & \text{in } \Omega_v, \\ \mathbf{W}_v^{\text{DB}}(\mathbf{x}, \mathbf{y}) &= \mathbf{0} & \text{on } \Gamma, \end{aligned} \right\} \quad (5.2)$$

where  $K^* = K_v \mu / d^2$ . Finally, the cell problem for the Stokes equation is [3]

$$\left. \begin{aligned} -\Delta_y \mathbf{W}_v^{\text{S}}(\mathbf{x}, \mathbf{y}) - \mathbb{I} + (\nabla_y \mathbf{g}_v^{\text{S}}(\mathbf{x}, \mathbf{y}))^T &= \mathbf{0} & \text{in } \Omega_v, \\ \nabla_y \cdot \mathbf{W}_v^{\text{S}}(\mathbf{x}, \mathbf{y}) &= 0 & \text{in } \Omega_v, \\ \mathbf{W}_v^{\text{S}}(\mathbf{x}, \mathbf{y}) &= \mathbf{0} & \text{on } \Gamma. \end{aligned} \right\} \quad (5.3)$$

We want to solve and compare the problems above in the cell domain  $\Omega_v$ ; therefore, we need to compare the same quantity at the macroscale. For Darcy–Brinkman and Stokes, the dimensionalized macroscopic velocity is given by (4.10):

$$\langle \mathbf{u}_v^{\text{DB/S}} \rangle_{\Omega_v} = -\frac{d^2}{\mu} \langle \mathbf{W}_v^{\text{DB/S}} \rangle_{\Omega_v} \nabla_x p^{(0)},$$

where  $\mathbf{W}_v^{\text{DB/S}}$  takes different expressions in Darcy–Brinkman's and Stokes' cases. On the other hand, for the Darcy case we have, by equation (4.12):

$$\langle \mathbf{u}_v \rangle_{\Omega_v} = -K^* \frac{d^2}{\mu} \langle \mathbb{I} + (\nabla_y \mathbf{g}_v)^T \rangle_{\Omega_v} \nabla_x p^{(0)}.$$

Hence we compare  $\langle \mathbf{W}_v^{\text{DB/S}} \rangle_{\Omega_v}$  for the Darcy–Brinkman and the Stokes problem and  $K^* \langle \mathbb{I} + (\nabla_y \mathbf{g}_v)^T \rangle_{\Omega_v}$  for the Darcy problem.

If we consider cylinders with a small radius, so that they have a small overlap region, we can analytically solve the previous systems up to a small error. The differential problems (5.2) and

(5.3) written in terms of the auxiliary tensor  $W_v$  can be shown to correspond to three standard Darcy–Brinkman and three Stokes' systems of equations, respectively, see also [10,39]. Using the rotation invariance property of our geometry, we can choose one arbitrary row (i.e. direction) of  $\mathbb{I}$ , say  $e_3$  (the third row of  $\mathbb{I}$ ), and we set  $W_{3,v} = W_v e_3$ . In this case, the solution is non-zero only in the branch directed along  $e_3$ , which means the only non-zero component is  $W_{3,v} e_3 = W_{33,v}$ .

Hence the solution of the system (5.3) is [39]

$$W_{33,v}^S = \frac{\hat{r}_c^2 - r^2}{4} \quad \text{and} \quad W_{31,v}^S = W_{32,v}^S = 0, \quad 0 \leq r \leq \hat{r}_c,$$

where  $\hat{r}_c$  is the radius of the cylinder (non-dimensional). Hence we have that the resulting permeability is

$$\langle W_{33,v}^S \rangle_{\Omega_v} = \frac{1}{|\Omega_v|} \int_0^{\hat{r}_c} dz \int_0^{2\pi} d\theta \int_0^{\hat{r}_c} \frac{\hat{r}_c^2 - r^2}{4} r dr = \frac{\pi l_c \hat{r}_c^4}{8|\Omega_v|}. \quad (5.4)$$

For the system (5.2), the problem reduces to

$$W_{33,v}^{\text{DB}''}(r) + \frac{1}{r} W_{33,v}^{\text{DB}'}(r) - \frac{W_{33,v}^{\text{DB}}(r)}{\mu^* K^*} = -\frac{1}{\mu^*}, \quad 0 \leq r \leq \hat{r}_c$$

and the solution is

$$W_{33,v}^{\text{DB}}(r) = K^* \left[ 1 - \frac{J_0\left(i\sqrt{(1/\mu^* K^*)}r\right)}{J_0\left(i\sqrt{(1/\mu^* K^*)}\hat{r}_c\right)} \right], \quad W_{31,v}^{\text{DB}} = W_{32,v}^{\text{DB}} = 0,$$

where  $J_0$  is the Bessel function of the first kind of order zero. Hence we have (using the property  $x^\nu J_{\nu-1} = (d/dx)(x^\nu J_\nu(x))$ ):

$$\begin{aligned} \langle W_{33,v}^{\text{DB}} \rangle_{\Omega_v} &= \frac{1}{|\Omega_v|} \int_0^{\hat{r}_c} dz \int_0^{2\pi} d\theta \int_0^{\hat{r}_c} K^* \left[ 1 - \frac{J_0\left(i\sqrt{(1/\mu^* K^*)}r\right)}{J_0\left(i\sqrt{(1/\mu^* K^*)}\hat{r}_c\right)} \right] r dr \\ &= \frac{2\pi l_c}{|\Omega_v|} K^* \left[ \frac{\hat{r}_c^2}{2} + i\sqrt{\mu^* K^*} \hat{r}_c \frac{J_1\left(i\sqrt{(1/\mu^* K^*)}\hat{r}_c\right)}{J_0\left(i\sqrt{(1/\mu^* K^*)}\hat{r}_c\right)} \right]. \end{aligned} \quad (5.5)$$

To solve system (5.1), we recall that  $\mathbf{n} = (n_1, n_2, 0) = (\cos \theta, \sin \theta, 0)$ . First of all, we focus on the case  $n_1 = \cos \theta$ , and we call the solution  $g_{v,1}$ . From the periodicity condition in the  $e_3$  direction, we have that  $g_v$  does not depend on the  $z$  variable. Hence the problem reduces to

$$\frac{1}{r} \frac{\partial}{\partial r} \left( r \frac{\partial g_{v,1}}{\partial r} \right) + \frac{1}{r^2} \frac{\partial^2 g_{v,1}}{\partial \theta^2} = 0, \quad 0 \leq r \leq \hat{r}_c, \quad 0 \leq \theta \leq 2\pi.$$

Using the separation of variables  $g_{v,1} = R(r)\Theta(\theta)$  and substituting into the equation above, we obtain

$$\left. \begin{aligned} r^2 R''(r) + rR'(r) - cR(r) &= 0, \\ \Theta''(\theta) + c\Theta(\theta) &= 0, \end{aligned} \right\} \quad (5.6)$$

where  $c$  is the constant obtained by the separation of variables. From the second equation of the system (5.6), we have

$$\Theta(\theta) = A \sin(n\theta) + B \cos(n\theta), \quad n \in \mathbb{N}.$$

From the boundary condition of the system (5.1), it follows that  $n = 1$ . Hence the solution of the first equation of the system (5.6) is

$$R(r) = \frac{C_1}{r} + C_2 r,$$

and, from the boundary condition of (5.1) and the non-degeneracy condition in  $r = 0$ , we have  $C_1 = 0$  and  $C_2 = 1$ . Hence we have

$$g_{v,1} = -r \cos \theta.$$

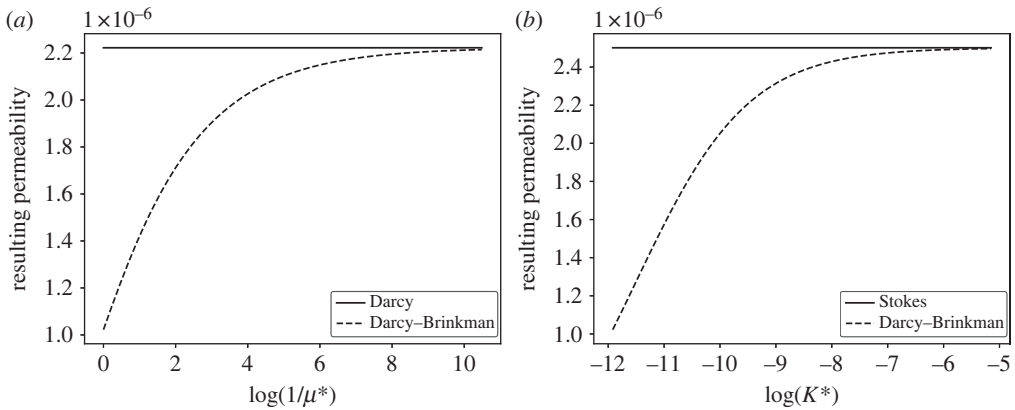


**Figure 3.** (a) Darcy–Brinkman/Darcy comparison with respect to  $1/\mu^*$ , for  $K^* = 6.67 \times 10^{-6}$ . (b) Darcy–Brinkman/Stokes comparison with respect to  $K^*$ , for  $\mu^* = 1$ .

**Table 1.** Comparison between Darcy–Brinkman and Darcy (left), Darcy–Brinkman and Stokes (right).

$\mu^*$	$K^*$	relative error
1	$6.67 \times 10^{-6}$	74%
$10^{-4}$	$6.67 \times 10^{-6}$	0.67%
$10^{-6}$	$6.67 \times 10^{-6}$	0.067%
1	$10^{-12}$	0.026%
1	$6.67 \times 10^{-6}$	84%
1	$10^{-4}$	9.5%
1	$10^{-2}$	0.1%
1	1	0.001%

In the same way, for the case  $n_2 = \sin \theta$  we get:

$$g_{v,2} = -r \sin \theta.$$

Hence it follows:

$$\langle (\nabla_y g_v)^T \rangle_{\Omega_v} = \frac{1}{|\Omega_v|} \int_{\Omega_v} (\nabla_y g_v)^T dV = -\frac{2}{3}. \quad (5.7)$$

These results are shown in figure 3, where we set  $\hat{r}_c = 7.7 \times 10^{-3}$ ,  $|\Omega_v| = 3\pi R^2 l_c$  (the volume is indeed a bit smaller, but we are supposing that the intersection between the cylinders is negligible).

As expected, the Darcy–Brinkman equation has a Stokes/Darcy duality behaviour. Indeed, suppose we decrease the relevance of the Laplace operator in the Darcy–Brinkman cell problem (5.2). In that case, we have that the solution tends to the solution of the Darcy cell problem (5.1). We can see this behaviour in figure 3a. The resulting permeability of the cell problem (5.2) tends to the one of the cell problem (5.1). We can see this behaviour even if we decrease the permeability instead of the relevance of the Laplace operator because, in this case, both the Darcy and the Darcy–Brinkman equations tend to zero. In figure 3b, we can see that if we increase  $K^*$  in the Darcy–Brinkman cell problem (5.2), the solution tends to that of the Stokes cell problem (5.3). Table 1 shows that, if the permeability is not too small or the Laplace operator is relevant, then the Darcy (resp. Stokes) and the Darcy–Brinkman equation give very different results; otherwise the solutions of the two problems are similar.

**Table 2.** Physiological and estimated parameters.

name	physiological range/value	description
$R$	0.49 mm	macroscopic radius [18,32]
$\mu$	$1 \text{ mg mm}^{-1} \text{ s}^{-1}$	viscosity [20,42]
$\phi$	0.75	porosity [29]
$\mu_e$	$\frac{\mu}{\phi}$	effective viscosity [5,43–45]
$\rho_0$	$1 \text{ mg mm}^{-3}$	density [20,42]
$\bar{K}_m$	$3.84 \times 10^{-9} \text{ mm}^2$	permeability of the interstitium [16,29]
$\sigma$	0.88–0.9	Staverman's coefficient [22,27,28,30]
$\pi_v - \pi_m$	$3.41 \times 10^5 - 2.08 \times 10^6 \text{ mPa}$	oncotic pressure difference [22,27,28,30,46–49]
$L_p$	$5.475 \times 10^{-12} - 3.67 \times 10^{-8} \text{ mm s}^{-1} \text{ mPa}^{-1}$	hydraulic conductivity of the blood vessel walls [22,27,28,30]
$\bar{p}_v$	$6.67 \times 10^5 - 1.066 \times 10^6 \text{ mPa}$	mean blood vessel pressure [22,27,28,30]
$S^{\text{tot}}$	$13.4 \text{ mm}^2$	blood vessel surface [23,24]
$ \Omega_v^{\text{tot}} $	$0.0322 \text{ mm}^3$	blood vessel volume [23]
$N$	1310	number of cells (electronic supplementary material, appendix B)
$r_c$	$1.7 \times 10^{-3} \text{ mm}$	microscale cylinders radius (electronic supplementary material, appendix B)
$d$	$2 \times 10^{-2} \text{ mm}$	microscale cylinders mean distance (electronic supplementary material, appendix B)
$L$	1 mm	coarse scale characteristic length
$c_0$	5.6	Kozeny constant [39]
$K_v \frac{d^2}{\mu}$	$1.1 \times 10^{-6} \text{ mm}^3 \text{ s mg}^{-1}$	hydraulic conductivity of the blood vessels using the Kozeny–Carman formula [50,51]
$f_m, f_v$	0	body forces
$\bar{K}_m$	$3.65 \times 10^{-9} \text{ mm}^3 \text{ s mg}^{-1}$	macroscopic interstitial hydraulic conductivity (solving system (3.29))
$\bar{K}_v$	$4.12 \times 10^{-7} \text{ mm}^3 \text{ s mg}^{-1}$	macroscopic blood hydraulic conductivity (solving system (3.24))

## 6. The explicit solution

In this section, we find an explicit solution to the macroscopic problem given in §4. More details about this section are given in electronic supplementary material, appendix A. For simplicity, we assume that the multiscale forces  $f_v^e$  and  $f_m^e$  vanish and that both porous media are isotropic, that is:

$$\bar{K}_v = \bar{K}_v \mathbb{I} \quad \text{and} \quad \bar{K}_m = \bar{K}_m \mathbb{I},$$

where, from equations (4.14) and (4.13),  $\bar{K}_v$  and  $\bar{K}_m$  correspond to  $(d^2/\mu)\langle \mathbf{K}_v + \mathbf{K}_v (\nabla_y \mathbf{g}_v)^T \rangle_{\Omega_v}$  and  $\langle (d^2/\mu) \mathbf{W}_m \rangle_{\Omega_m}$ , respectively. We recall that the base value for the dimensional vessels' hydraulic conductivity  $K_v d^2/\mu$  is computed according to the Kozeny Carman model, i.e.  $\frac{1}{c_0 \left( \frac{S^{\text{tot}}}{|\Omega_v^{\text{tot}}|} \right)^2}$ , see

table 2 and supplementary material, appendix B for further details. We have that  $\bar{K}_v$  and  $\bar{K}_m$  are constants due to the geometry and the hypotheses used, and they are found solving the cell

problems (3.24) and (3.29), respectively, using COMSOL Multiphysics, with  $\alpha = 1$  (see electronic supplementary material, appendix C for more details). We consider a spherical domain  $\Omega$ , denoting by  $r$  the radial coordinate,  $\theta$  the polar coordinate, and  $\phi$  the azimuthal angle. Moreover, we assume axisymmetry with respect to the azimuthal angle  $\phi$ . Hence our problem is:

$$\left. \begin{aligned} \Delta p_v(r, \theta) &= -M_v[p_m(r, \theta) - p_v(r, \theta) - \bar{p}] & r < R, \theta \in [0, 2\pi[, \\ \Delta p_m(r, \theta) &= M_m[p_m(r, \theta) - p_v(r, \theta) - \bar{p}] & r < R, \theta \in [0, 2\pi[, \\ p_v(R, \theta) &= \bar{p}_v(\theta), \quad p_m(R, \theta) = \bar{p}_m(\theta) & \theta \in [0, 2\pi[, \\ \text{non-degeneracy} & & r = 0, \theta \in [0, 2\pi[, \end{aligned} \right\} \quad (6.1)$$

where  $R$  is the radius of the spherical domain,  $M_v = L_p S^{\text{tot}} / (|\Omega_v^{\text{tot}}| \bar{K}_v)$ , and  $M_m = L_p S^{\text{tot}} / (|\Omega_m^{\text{tot}}| \bar{K}_m)$ .

We define the quantity

$$\psi(r, \theta) = p_m(r, \theta) - p_v(r, \theta), \quad (6.2)$$

and, taking the difference between the second and the first equation of the system (6.1), we obtain the new problem

$$\left. \begin{aligned} \Delta \psi(r, \theta) &= M[\psi(r, \theta) - \bar{p}] & r < R, \theta \in [0, 2\pi[, \\ \psi(R, \theta) &= \bar{p}_m(\theta) - \bar{p}_v(\theta), & \theta \in [0, 2\pi[, \\ \text{non-degeneracy} & & r = 0, \theta \in [0, 2\pi[, \end{aligned} \right\} \quad (6.3)$$

where  $M = M_v + M_m$ . Defining

$$\hat{\psi}(r, \theta) = \psi(r, \theta) - \bar{p}, \quad (6.4)$$

we can reformulate the first equation of the system (6.3) as

$$\Delta \hat{\psi}(r, \theta) = M \hat{\psi}(r, \theta). \quad (6.5)$$

Details about the computations can be found in electronic supplementary material, appendix A. The solution to the problem (6.5) is the following:

$$\hat{\psi}(r, \zeta) = \sum_{n=0}^{\infty} \tilde{A}_n \frac{1}{\sqrt{r}} I_{n+(1/2)}(\sqrt{Mr}) P_n(\zeta), \quad (6.6)$$

where  $\zeta = \cos \theta$ ,  $I_{n+(1/2)}$  is the *modified Bessel polynomial of the first kind*,  $P_n(\zeta)$  is the *Legendre polynomial of the first kind* [40], and with the boundary condition from the second equation in the system (6.3)

$$\psi(R, \zeta) = \bar{p}_m(\zeta) - \bar{p}_v(\zeta) = \sum_{n=0}^{\infty} b^{(n)} P_n(\zeta). \quad (6.7)$$

We have that  $\tilde{A}_n$  is given by the boundary conditions (6.7), and it is

$$\tilde{A}_0 = \frac{[b^{(0)} - \bar{p}] \sqrt{R}}{I_{\frac{1}{2}}(\sqrt{MR})} \quad \text{for } n=0, \quad \tilde{A}_n = \frac{b^{(n)} \sqrt{R}}{I_{n+\frac{1}{2}}(\sqrt{MR})} \quad \text{for } n \in \mathbb{N}, n \neq 0. \quad (6.8)$$

The solutions of the system (6.1) are

$$p_m(r, \zeta) = \sum_{n=0}^{\infty} \left[ c_1^{(n)} r^n + \frac{M_m \tilde{A}_n}{M} \frac{1}{\sqrt{r}} I_{n+(1/2)}(\sqrt{Mr}) \right] P_n(\zeta) \quad (6.9)$$

and

$$p_v(r, \zeta) = \sum_{n=0}^{\infty} \left[ d_1^{(n)} r^n - \frac{M_v \tilde{A}_n}{M} \frac{1}{\sqrt{r}} I_{n+(1/2)}(\sqrt{Mr}) \right] P_n(\zeta), \quad (6.10)$$

where the constants  $c_1^{(n)}$  and  $d_1^{(n)}$  are found explicitly in electronic supplementary material, appendix A.

## 7. Application to the lymph node

In this section, we show the results given by the explicit solution with physiological data obtained or estimated by an idealized spherical mouse popliteal lymph node [32]. The lymph node is basically formed by two parts: a porous bulk region called LC and a thin layer against the wall where the fluid can flow freely, called subcapsular sinus (SCS) [11,41]. Owing to the fact that the whole blood vasculature in the lymph node is in the LC [22–24], in this section, we apply the explicit solution found in the previous section to the LC, implemented in Matlab.

Here we have that  $\Omega_v$  is the *blood vessels phase*, and  $\Omega_m$  is the *interstitial phase*. The fluid exchange between these two phases is described by the Starling equation, which corresponds to choose  $\bar{p} = \sigma(\pi_m - \pi_v)$ . The physiological data used in this work are explained in electronic supplementary material, appendix B and are summarized in table 2.

To find the hydraulic conductivity  $\bar{K}_v$  and  $\bar{K}_m$  of the dimensional macroscale equations (4.12) and (4.10) defined in (4.15) and (4.14), we solve the cell problems (3.25) and (3.30) with the body forces  $\mathbf{f}_m = \mathbf{f}_v = \mathbf{0}$ ,  $\alpha = 1$ , and using the microstructure parameters described in table 2, using COMSOL Multiphysics (see electronic supplementary material, appendix C for more information about the numerical simulations). In [22], they used an interstitial hydraulic conductivity similar to those measured in LS174T tumours of the value of  $\approx 2 \times 10^{-10} \text{ mm}^3 \text{ s}^{-1} \text{ mg}^{-1}$ . In [27], they found an average permeability of  $\approx 3.8 \times 10^{-5} \text{ mm}^2$  fitting the results found in their model to the data of a canine popliteal lymph node from Adair & Guyton [46]. In our model, we obtained the hydraulic conductivity  $\bar{K}_m = 3.65 \times 10^{-9} \text{ mm}^3 \text{ s}^{-1} \text{ mg}^{-1}$ , starting with a permeability of  $3.84 \times 10^{-9} \text{ mm}^2$  for the Darcy-Brinkman equation, taken from [16,29]. The strength of our model is to obtain a permeability for the macroscale using a rigorous homogenization method (i.e. asymptotic homogenization), taking into account the geometry and the differential equations used in the microscale. Moreover, we found the hydraulic conductivity and the fluid flow inside the blood vessels too in order to better describe the fluid exchange between the blood vessels and the lymph.

As boundary conditions we choose:

$$p_v(R, \zeta) = \bar{p}_v \quad \text{and} \quad p_m(R, \zeta) = \bar{p}_m(\zeta),$$

where  $\bar{p}_v$  is a constant value given by the literature (mean blood vessels pressure), and  $\bar{p}_m(\zeta)$  can be any function sufficiently regular of  $\zeta$ .

To begin with (and for simplicity), we assume that  $\bar{p}_m(\zeta) = \bar{p}_m$  is a fixed constant value. In this case, we can see the direction of the fluid exchange between the interstitial space and the blood vessels explicitly. Indeed, in this case, remains only the  $n = 0$  term (from equations (6.7), the computations in electronic supplementary material, appendix A, and from the fact that  $P_0(x) = 1$  we have  $b^{(0)} = b_m^{(0)} - b_n^{(0)} = \bar{p}_m - \bar{p}_v$ ), and this implies that equation (6.6) reduces to

$$\hat{\psi}(r) = \tilde{A}_0 \frac{I_{1/2}(\sqrt{M}r)}{\sqrt{r}} = \frac{\sqrt{R}I_{1/2}(\sqrt{M}r)}{\sqrt{r}I_{1/2}(\sqrt{MR})} [\bar{p}_m - \bar{p}_v - \sigma(\pi_m - \pi_v)].$$

From the fact that (4.5) can be written as  $\nabla_x \cdot \langle \mathbf{u}_v^{(0)}(x, \mathbf{y}) \rangle_{\Omega_v} = (L_p S^{\text{tot}} / |\Omega_v^{\text{tot}}|) \hat{\psi}(r)$  and recalling that  $I_{1/2}(x) = \sqrt{(2/\pi)} \sinh(x) / \sqrt{x}$  is positive for every  $x > 0$ , we have that the divergence in (4.5) has the same sign as

$$\bar{p}_m - \bar{p}_v - \sigma(\pi_m - \pi_v), \quad (7.1)$$

which is the opposite sign of the divergence in (4.3); this gives us information about the direction of the fluid exchange.

The work [52] measured that the average pressure in a lymph node is about  $6.86 \pm 0.56 \text{ cmH}_2\text{O} \approx 6.7 \times 10^5 \pm 5.5 \times 10^4 \text{ mPa}$ , so, for now, we fix  $\bar{p}_m = 6.7 \times 10^5 \text{ mPa}$ . With this value,  $\sigma = 0.88$  and  $\Delta\pi = 1.02 \times 10^6 \text{ mPa}$ , we have that the sign of (7.1) is negative for  $\bar{p}_v \lesssim 1.5676 \times 10^6 \text{ mPa} \approx 11.8 \text{ mmHg}$  (which means that the fluid goes from the interstitial space to the blood phase), and start to have an inversion of the flow at  $\bar{p}_v \approx 1.5676 \times 10^6 \text{ mPa} \approx 11.8 \text{ mmHg}$ .



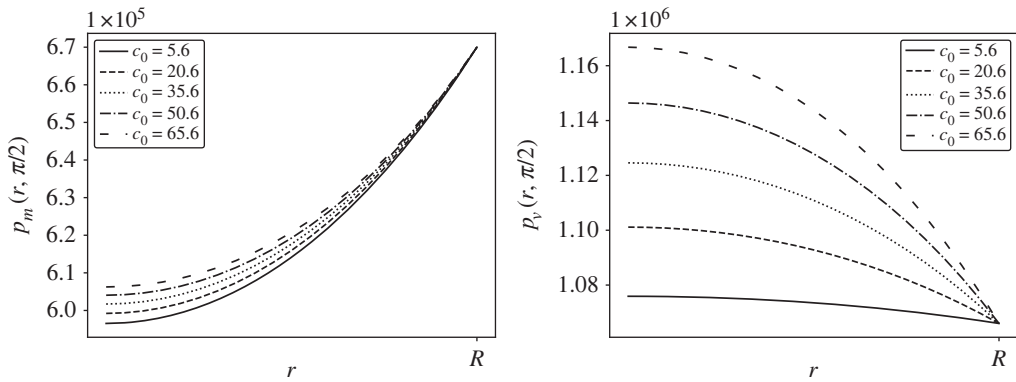


**Figure 4.** The variation of  $p_m$  and  $p_v$  in mPa at  $\theta = \pi/2$ , for some values of the Kozeny constant  $c_0$ , with  $\pi_v - \pi_m = 1.02 \times 10^6$  mPa,  $\bar{p}_v = 1.066 \times 10^6$  mPa,  $L_p = 5.475 \times 10^{-10}$  mm s $^{-1}$  mPa $^{-1}$ ,  $\bar{p}_m = 6.7 \times 10^5$  mPa and the parameters in table 2.

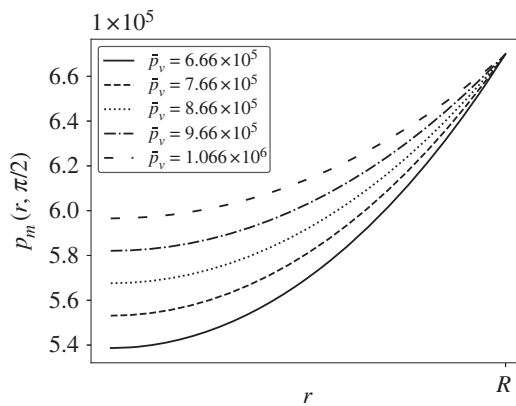


**Figure 5.** The variation of  $p_m$  in mPa at  $\theta = \pi/2$ , for some values of the blood vessel pressure  $\bar{p}_v$  in mPa, with  $\pi_v - \pi_m = 1.02 \times 10^6$  mPa,  $L_p = 5.475 \times 10^{-10}$  mm s $^{-1}$  mPa $^{-1}$ ,  $\bar{p}_m = 6.7 \times 10^5$  mPa and the parameters in table 2.

In figure 4, we can see the resulting pressures  $p_m$  and  $p_v$  varying with respect to the Kozeny constant  $c_0$ . In this case, the range specified in figure 4 is used for  $c_0$  rather than solely the base value reported in table 2. Increasing  $c_0$  means increasing the tortuosity of the blood vessels [39], and this is related to an increase of  $p_v$  and  $p_m$  at the centre of the node, and that means that there is less flow from the interstitial space to the blood vessels (remembering that Darcy's Law linearly relates the fluid discharge to the pressure difference, so the lymph moves accordingly to the pressure, see figure 12 and below for more details). This is related to the fact that increasing  $c_0$  in the Kozeny–Carman formula (electronic supplementary material, appendix B) means a decrease in  $K_v$ . Consequently, an increase of the pressure  $p_v$  at the centre of the node means an increase of  $p_m$ ; we can see this behaviour better in figure 5. This is a parametric study with the variation of  $c_0$  related to the tortuosity effect [39]; however, to study the role of the tortuosity in more detail, we need to take it into account in the geometry of the microscale problem, which we did not do in this case.

In figure 6, we can see the resulting pressures  $p_m$  and  $p_v$  varying with respect to the hydraulic conductivity of the blood vessel walls  $L_p$ . Increasing  $L_p$  means a decrease of  $p_m$  and an increase of  $p_v$  at the centre of the node, meaning a higher flow from the interstitial space to the blood vessels (as expected).

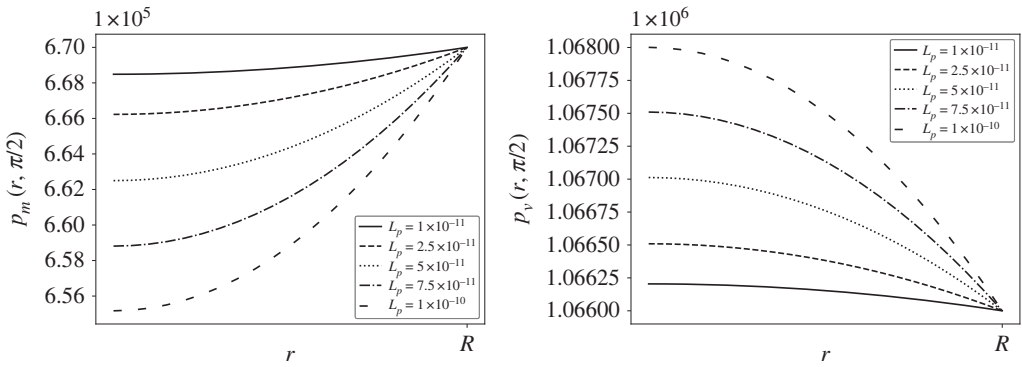


**Figure 6.** The variation of  $p_m$  and  $p_v$  in mPa at  $\theta = \pi/2$ , for some values of the hydraulic conductivity  $L_p$  in  $\text{mm s}^{-1} \text{mPa}^{-1}$ , with  $\pi_v - \pi_m = 1.02 \times 10^6$  mPa,  $\bar{p}_v = 1.066 \times 10^6$  mPa,  $\bar{p}_m = 6.7 \times 10^5$  mPa and the parameters in table 2.

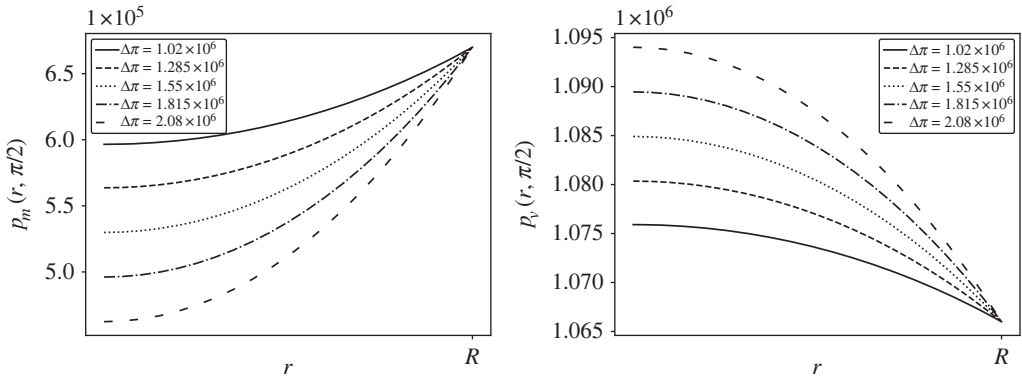


**Figure 7.** The variation of  $p_m$  and  $p_v$  in mPa at  $\theta = \pi/2$ , for some values of the oncotic pressure difference  $\Delta\pi = \pi_v - \pi_m$  in mPa, with  $\bar{p}_v = 1.066 \times 10^6$  mPa,  $L_p = 5.475 \times 10^{-10}$   $\text{mm s}^{-1} \text{mPa}^{-1}$ ,  $\bar{p}_m = 6.7 \times 10^5$  mPa and the parameters in table 2.

In figure 7, we can see the resulting pressures  $p_m$  and  $p_v$  varying with respect to  $\Delta\pi = \pi_v - \pi_m$ . Increasing  $\Delta\pi$  means increasing the concentration difference between the interstitial space and the blood vessels, and consequently the increase of the fluid flow from  $\Omega_m$  to  $\Omega_v$ .

The strength of the explicit solution we found in §6 is to take into account the variation with respect to  $\theta$  of the boundary condition  $\bar{p}_m$  to mimic the pressure distribution in the SCS. Unfortunately, as far as we know, there are no precise physiological data available for the pressure distribution in the SCS. Hence, inspired by Grebennikov *et al.* [15], we take a linear variation of the pressure along the  $\theta$  coordinate between the values  $\bar{p}_{m,\max} = 3.9 \text{ mmHg} \approx 5.2 \times 10^5$  mPa and  $\bar{p}_{m,\min} = 3 \text{ mmHg} \approx 4 \times 10^5$  mPa; these values are taken from the resulting pressure in [22]. Hence we can write:

$$\bar{p}_m(\zeta) = \bar{p}_{m,\min} + \frac{\zeta + 1}{2}(\bar{p}_{m,\max} - \bar{p}_{m,\min}). \quad (7.2)$$

Given this boundary condition, if we use the physiological values used in [22] ( $\sigma = 0.88$  and  $\pi_v - \pi_m = 1.02 \times 10^6$  mPa), we have an inversion of the flow at  $\approx 1.4 \times 10^6$  mPa  $\approx 10.5$  mmHg, the same found in [22]. We can see this behaviour in figure 8.

In figure 9, we show the interstitial pressure distribution in the whole domain (recalling that we assume axisymmetry) varying the hydraulic conductivity of the blood vessel walls  $L_p$ . As we can see, we have that the position and the value of the minimum of the pressure vary

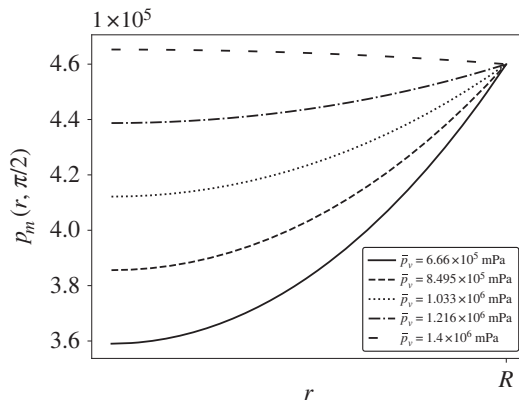


**Figure 8.** The variation of  $p_m$  in mPa at  $\theta = \pi/2$ , for some values of the mean blood vessel pressure  $\bar{p}_v$  in mPa, with  $\pi_v - \pi_m = 1.02 \times 10^6$  mPa,  $L_p = 5.475 \times 10^{-10}$  mm s<sup>-1</sup> mPa<sup>-1</sup>, the boundary conditions (7.2) and the parameters in table 2.

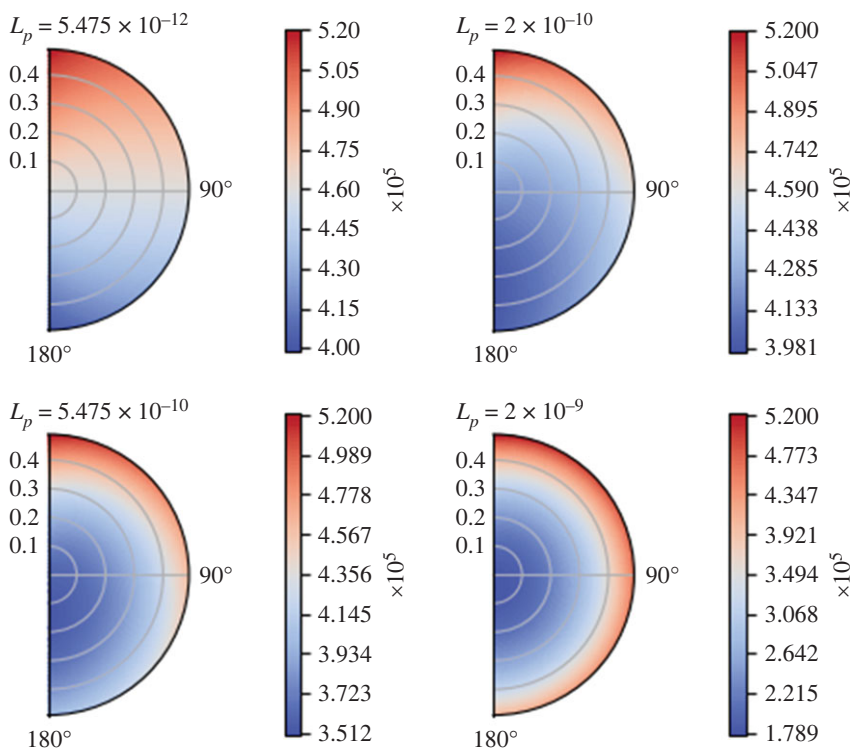


**Figure 9.** The variation of  $p_m$  in mPa in all the domain, for some values of  $L_p$ , with  $\pi_v - \pi_m = 1.02 \times 10^6$  mPa,  $\bar{p}_v = 6.66 \times 10^6$  mPa, the boundary conditions (7.2) and the parameters in table 2.

with respect to  $L_p$ ; as  $L_p$  increases, the minimum of the pressure decreases (figure 6) and moves towards the centre of the node. This is due to a combination of the pressure variation given by the boundary conditions (7.2) and the fluid exchange between phases. These results confirm that the  $\theta$  dependence in our explicit solution is essential to describe the fluid motion and the pressure distribution inside a lymph node. The value of the minimum pressure is related to a sink term due

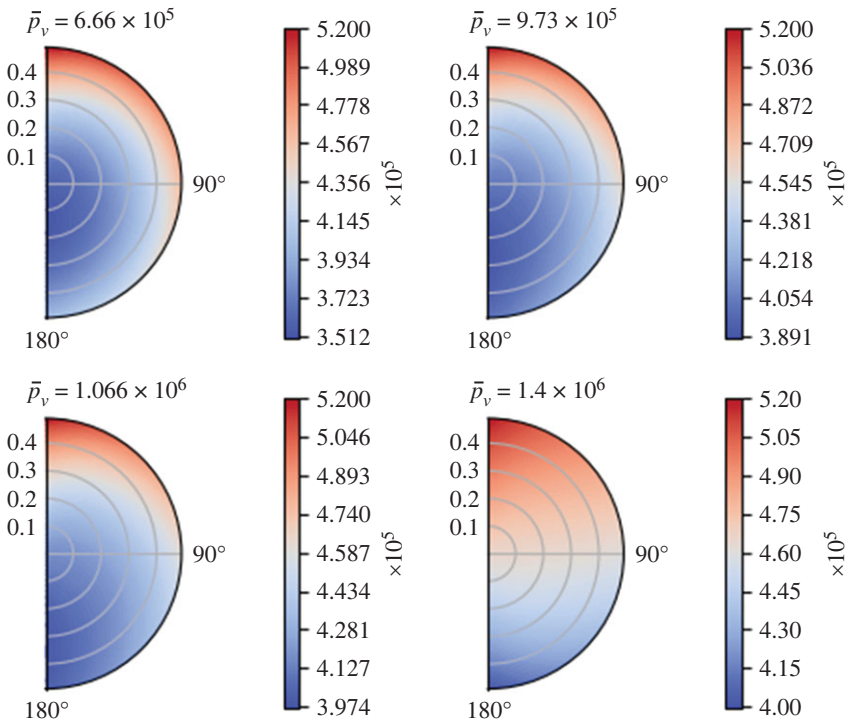


**Figure 10.** The variation of  $p_m$  in mPa in all the domain, for some values of  $\bar{p}_v$  in mPa, with  $\pi_v - \pi_m = 1.02 \times 10^6$  mPa,  $L_p = 5.475 \times 10^{-10}$  mm s $^{-1}$  mPa $^{-1}$  the boundary conditions (7.2) and the parameters in table 2.

to the blood vessel's drainage function; here we have that the blood vessel's effect is less relevant with respect to the one found in [22], but the behaviour is the same. This is in line with the results of [22], because the permeability that we obtain with our multiscale formulation is bigger than the one used by them.

In figure 10, we can see the interstitial pressure distribution in the whole domain varying the blood vessel pressure  $\bar{p}_v$ . As we can see, we have that increasing  $\bar{p}_v$  increases the minimum of the pressure  $p_m$  and moves the minimum from the centre to the lower part ( $\zeta = -1$  where we have the minimum in equation (7.2)) of the node. This behaviour is the opposite of what we have in figure 9, in accordance with the results found in figures 5 and 6.

As we mentioned before, we can choose as boundary condition  $\bar{p}_m(\zeta)$  what we want; hence we can choose the more complicated pressure distribution found with the stream function approach in the steady case (see [53] for more details):

$$\bar{p}_m(R, \zeta) = C_{\text{steady}} - \mu \sum_{n=1}^{\infty} \left[ \frac{2(2(n+1)+1)}{n} C_n^s R^n + \frac{2(2(n+1)-3)}{n+1} D_n^s R^{-n-1} \right] P_n(\zeta) \quad (7.3)$$

where the constants  $C_{\text{steady}}$ ,  $C_n^s$  and  $D_n^s$  are calculated in [32] in a steady case without fluid-exchange (div-free solution), where we fix the pressure at one point  $\bar{p}_m(R_2, -1) = 6.18 \times 10^5$  mPa and with an inlet and outlet boundary condition defined in the domain  $[-1, -1 + \zeta_0]$  (outlet condition) and  $[1 - \zeta_0, 1]$  (inlet condition), where  $\zeta_0 = \cos[\arcsin(R_{LV}/\sqrt{R_{LV}^2 + R_2^2})] = R_2/\sqrt{R_{LV}^2 + R_2^2}$ ,  $R_{LV} = 0.04$  mm and  $R_2 = 0.5$  mm. The boundary pressure distribution is plotted in figure 11. We can see that we have a fast increment of pressure near the inlet boundary condition (and a fast decrement near the outlet boundary condition). With these boundary conditions and the parameters  $\bar{p}_v = 1.06 \times 10^6$  mPa,  $\pi_v - \pi_m = 1.02 \times 10^6$  mPa and  $L_p = 5.475 \times 10^{-11}$  mm s $^{-1}$  mPa $^{-1}$ , we obtain the pressure and the velocity distribution shown in figure 12.

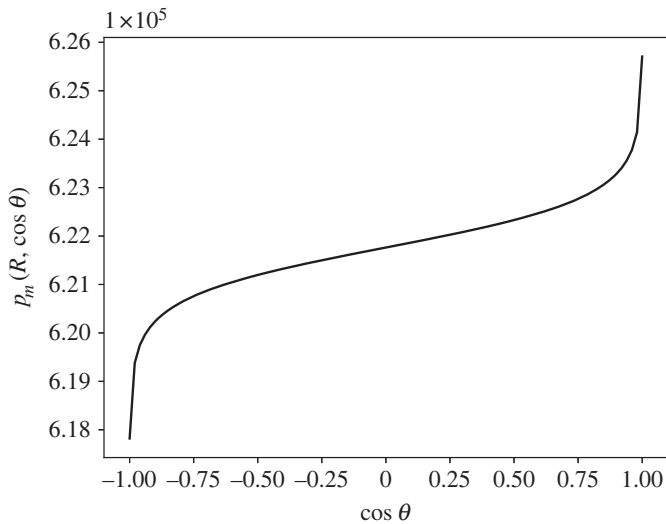


**Figure 11.** The pressure distribution in mPa of equation (7.3) with the values calculated in [32].

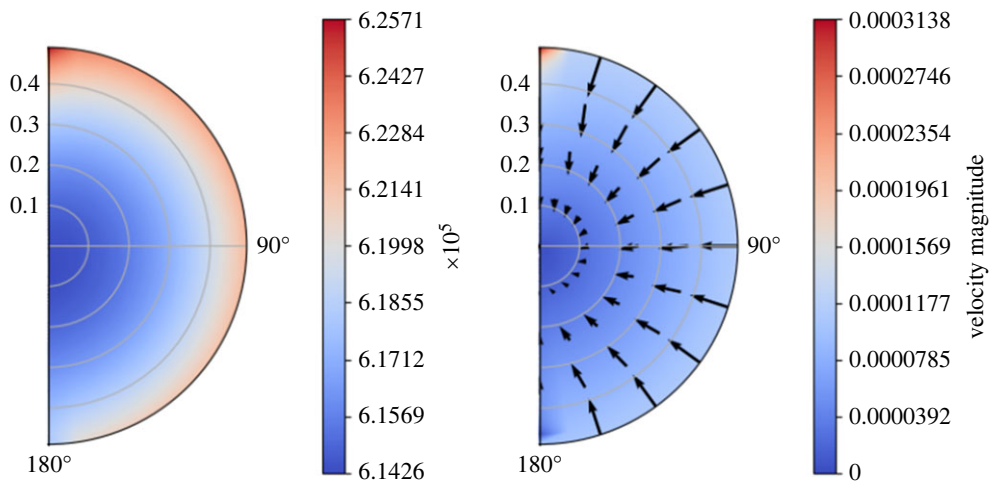


**Figure 12.** The pressure distribution of  $p_m$  (left) in mPa and the velocity distribution (right) in  $\text{mm s}^{-1}$  with boundary conditions (7.3) (values calculated in [32]),  $\bar{p}_v = 1.06 \times 10^6$  mPa,  $\pi_v - \pi_m = 1.02 \times 10^6$  mPa and  $L_p = 5.475 \times 10^{-11} \text{ mm s}^{-1} \text{ mPa}^{-1}$ .

Varying the parameters that regulate the fluid exchange, we obtain the same behaviour obtained above. As we can see, we have a pressure distribution similar to those found earlier, but we have a higher (lower) pressure distribution near the inlet (outlet), and we have the same behaviour for the velocity magnitude. In this case, we have an inversion of flow with the mean blood vessels pressure  $\bar{p}_v \approx 1.53 \times 10^6$  mPa  $\approx 11.476$  mmHg, similar to the one found with the constant value  $\bar{p}_m \approx 6.7 \times 10^5$  mPa. The pressure values found here are in range with the ones measured in [52] and found in [32]. In this case, instead of observing a pressure gradient that varies from a high-pressure region near the inlet to a low-pressure region near the outlet, we find that the low-pressure zone is closer to the centre of the LC. This particular region experiences reduced pressure due to the exchange of fluids between lymph and blood vessels, and this phenomenon is represented by a sink term. Owing to this, we have that lymph moves toward the low-pressure

zone in the centre of the node, and we can see this from the velocity plot in figure 12. Moreover, the velocity behaviour is very similar to the one found in [22], although the velocities found here are slightly higher: this is due to the fact that we used a higher  $L_p$  than the one used by them and because we found a higher hydraulic conductivity.

## 8. Conclusion

In this article, we have proposed a macroscopic model using the asymptotic homogenization technique resulting from the starting equations (2.1) and (2.2) and the interface condition (2.3), which account for blood transcappillary exchange across the vessels walls, under the assumption of local periodicity and macroscopic uniformity in a steady setting. Our starting point is the Darcy/Darcy–Brinkman equation, so we have considered the pore structure already smoothed out, and that simplifies the model because we do not need precise information about the microscale geometry (this information is encoded in the hydraulic conductivity  $\hat{K}_\gamma$ ,  $\gamma = m, v$ ). After that, in §5 we have analysed in detail the differences between using Darcy, Darcy–Brinkman or Stokes as our starting point, and we have found that the Darcy–Brinkman equation has a Darcy–Stokes duality behaviour depending on the value of the permeability (and the relevance of the Laplace operator). Although it is less theoretically justified than the Darcy equation, the Darcy–Brinkman equation is a valid starting point for our multiscale formulation since we have a Stokes-like structure of the differential equation, which allow us to specify in more detail the boundary condition without the need for a precise structure of the microscale, which is described by the permeability parameter (that in most cases is easier to obtain). Moreover, the coupling between the Darcy and Darcy–Brinkman equation has allowed the separation of the cell problem into two distinct phases, one involving the blood vessels and the other involving the FRC network so that we could solve the cell problems in the two domains separately.

After this model analysis, in §6 we have found the macroscopic explicit solution of the resulting equation of the proposed model (described in §4) in a spherical domain (under certainly simplified hypothesis) in terms of Bessel and Legendre polynomials. Then, in §7 we have applied this explicit solution to an idealized spherical lymph node using physiological data from the literature; our multiscale formulation of the problem has allowed us to study the fluid behaviour in the interstitial space and in the blood vessels within the node, allowing us to study the interaction and the fluid exchange between these two phases in more detail. We have mainly focused on the porous part of the lymph node (the LC) and on the fluid exchange between the interstitial space of the lymph node and the blood vessels, which are only in this part of the node [22–24]; despite the blood vessel pressure being higher than the interstitial pressure of the node, we have that the blood vessels have a higher concentration of protein too, and this leads to the fact that the lymph goes from the node to the blood circulation, making the lymph nodes important in the fluid regulation within the lymphatic system [21]. We have analysed how the parameters affect the fluid absorption and the pressure (i.e. the velocity) with different boundary pressure, and the behaviour of the results is in line with those found in the literature [22,46–48,52].

The current work is open for improvements. First of all, in this analysis, we have considered only the LC and we have supposed a given pressure of the SCS; in general, we need to couple these two motions.

We have assumed that the multiscale forces vanished when we applied our model to a lymph node for the sake of simplicity. In general, these forces can be relevant, for example, when electromagnetic fields are used (see, e.g. [54,55] in the context of cancer hyperthermia) so that the role of inhomogeneous volume loads as considered in [10] should be considered when physiological data become available.

We study the fluid flow in a steady case, but in general, we have a time dependence of the flow given by the time-pulsation of the lymphangion [20,42,56]; it will be of crucial importance to address this aspect in future works [31,32].

Finally, we have proposed to use a spherical geometry for the sake of simplicity and to find an explicit solution, but, in general, the LNs are not characterized by a spherical shape

and it is reportedly more similar to an ellipsoid [22,27,28,31]. Assuming that more realistic information concerning the shape, e.g. suggested by medical images, become available, our modelling framework could be in future exploited to compute the macroscale solution of the model numerically in order to formulate physiologically relevant predictions.

**Data accessibility.** Additional data are provided in electronic supplementary material [57].

**Authors' contributions.** A.G.: data curation, formal analysis, investigation, methodology, software, writing—original draft, writing—review and editing; G.G.: conceptualization, investigation, methodology, supervision, writing—review and editing; A.M.: conceptualization, investigation, methodology, supervision, writing—review and editing; R.P.: conceptualization, investigation, methodology, project administration, supervision, writing—review and editing.

All authors gave final approval for publication and agreed to be held accountable for the work performed therein.

**Conflict of interest declaration.** We declare we have no competing interests.

**Funding.** This work was partially supported by National Group of Mathematical Physics (GNFM-INdAM). R.P. is partially funded by EPSRC grant nos. EP/S030875/1 and EP/T017899/1.

**Acknowledgements.** The authors thank the anonymous reviewers for their comments and suggestions.

## References

1. Darcy H. 1856 *Les fontaines publiques de la ville de Dijon*. Paris: Victor Dalmont.
2. Rajagopal KR. 2007 On a hierarchy of approximate models for flows of incompressible fluids through porous solids. *Math. Models Methods Appl. Sci.* **17**, 215–252. (doi:10.1142/S0218202507001899)
3. Hornung U. 1997 *Homogenization and porous media*. Springer Science+Business Media. New York, NY: Springer.
4. Gerisch A, Penta R, Lang J. 2018 *Multiscale models in mechano and tumor biology*. (Gewerbstrasse 11, 6330). Cham, Switzerland: Springer.
5. Brinkman H. 1949 A calculation of the viscous force exerted by a flowing fluid on a dense swarm of particles. *Appl. Sci. Res.* **A1**, 27–34. (doi:10.1007/BF02120313)
6. Marusic-Paloka E, Pazanin I, Marusic S. 2012 Comparison between Darcy and Brinkman laws in a fracture. *Appl. Math. Comput.* **218**, 7538–7545. (doi:10.1016/j.amc.2012.01.021)
7. Naele G, Nader W. 1974 Practical significance of Brinkman's extension of Darcy's law: coupled parallel flows within a channel and a bounding porous medium. *Can. J. Chem. Eng.* **52**, 475–478.
8. Auriault JL, Geindreau C, Boutin C. 2005 Filtration law in porous media with poor separation of scales. *Transp. Porous Media* **60**, 89–108. (doi:10.1007/s11242-004-3649-7)
9. Lèvy T. 1983 Fluid flow through an array of fixed particles. *Int. J. Eng. Sci.* **21**, 11–23. (doi:10.1016/0020-7225(83)90035-6)
10. Penta R, Ramírez-Torres AD, Merodio J, Rodríguez-Ramos R. 2020 Effective governing equations for heterogeneous porous media subject to inhomogeneous body forces. *Math. Eng.* **3**, 1–17. (doi:10.3934/mine.2021033)
11. O'Melia MJ, Lund AW, Thomas SN. 2019 The biophysics of lymphatic transport: engineering tools and immunological consequences. *Iscience* **22**, 28–43. (doi:10.1016/j.isci.2019.11.005)
12. Arasa J, Collado-Diaz V, Halin C. 2021 Structure and immune function of afferent lymphatics and their mechanistic contribution to dendritic cell and T cell trafficking. *Cells* **10**, 1269. (doi:10.3390/cells10051269)
13. Novkovic M, Onder L, Bocharov G, Ludewig B. 2020 Topological structure and robustness of the lymph node conduit system. *Cell Rep.* **30**, 893–904. (doi:10.1016/j.celrep.2019.12.070)
14. Roozendaal R, Mebius RE, Kraal G. 2008 The conduit system of the lymph node. *Int. Immunol.* **20**, 1483–1487. (doi:10.1093/intimm/dxn110)
15. Grebennikov D, Van Loon R, Novkovic M, Onder L, Savinkov R, Sazonov I, Tretyakova R, Watson DJ, Bocharov G. 2016 Critical issues in modelling lymph node physiology. *Computation* **5**, 3. (doi:10.3390/computation5010003)
16. Savinkov R, Kislitsyn A, Watson DJ, van Loon R, Sazonov I, Novkovic M, Onder L, Bocharov G. 2017 Data-driven modelling of the FRC network for studying the fluid flow in the conduit system. *Eng. Appl. Artif. Intell.* **62**, 341–349. (doi:10.1016/j.engappai.2016.10.007)
17. Apoorva Fet al. 2018 How biophysical forces regulate human B cell lymphomas. *Cell Reports* **23**, 499–511. (doi:10.1016/j.celrep.2018.03.069)

18. Birmingham KG, O'Melia MJ, Bordy S, Aguilar DR, El-Reyas B, Lesinski G, Thomas SN. 2020 Lymph node subcapsular sinus microenvironment-on-a-chip modeling shear flow relevant to lymphatic metastasis and immune cell homing. *Iscience* **23**, 101751. (doi:10.1016/j.isci.2020.101751)
19. Permana AD, Nainu F, Moffatt K, Larrañeta E, Donnelly RF. 2021 Recent advances in combination of microneedles and nanomedicines for lymphatic targeted drug delivery. *Wiley Interdiscip. Rev. Nanomed. Nanobiotechnol.* **13**, e1690. (doi:10.1002/wnan.1690)
20. Moore Jr JE, Bertram CD. 2018 Lymphatic system flows. *Annu. Rev. Fluid Mech.* **50**, 459–482. (doi:10.1146/annurev-fluid-122316-045259)
21. Tobbia D, Semple J, Baker A, Dumont D, Semple A, Johnston M. 2009 Lymphedema development and lymphatic function following lymph node excision in sheep. *J. Vasc. Res.* **46**, 426–434. (doi:10.1159/000194273)
22. Jafarnejad M, Woodruff MC, Zawieja DC, Carroll MC, Moore Jr J. 2015 Modeling lymph flow and fluid exchange with blood vessels in lymph nodes. *Lymphat. Res. Biol.* **13**, 234–247. (doi:10.1089/lrb.2015.0028)
23. Jafarnejad M, Ismail AZ, Duarte D, Vyas C, Ghahramani A, Poologasundarampillai Jr G, Moore JE. 2019 Quantification of the whole lymph node vasculature based on tomography of the vessel corrosion casts. *Nat. Sci. Rep.* **9**, 13380. (doi:10.1038/s41598-019-49055-7)
24. Kelch ID, Bogle G, Sands GB, Phillips ARJ, LeGrice IJ, Dunbar PR. 2015 Organ-wide 3D-imaging and topological analysis of the continuous microvascular network in a murine lymph node. *Nat. Sci. Rep.* **5**, 16534. (doi:10.1038/srep16534)
25. Novkovic M, Onder L, Cheng HW, Bocharov G, Ludewig B. 2018 Integrative computational modeling of the lymph node stromal cell landscape. *Front. Immunol.* **9**, 2428. (doi:10.3389/fimmu.2018.02428)
26. Shanti A, Teo J, Stefanini C. 2018 In vitro immune organs-on-chip for drug development: a review. *Pharmaceutics* **10**, 278. (doi:10.3390/pharmaceutics10040278)
27. Cooper LJ, Heppell JP, Clough GF, Ganapathisubramani B, Roose T. 2016 An image-based model of fluid flow through lymph nodes. *Bull. Math. Biol.* **78**, 52–71. (doi:10.1007/s11538-015-0128-y)
28. Cooper L, Zeller-Plumhoff B, Clough G, Ganapathisubramani B, Roose T. 2018 Using high resolution X-ray computed tomography to create an image based model of a lymph node. *J. Theor. Biol.* **449**, 73–82. (doi:10.1016/j.jtbi.2018.04.021)
29. Shanti A *et al.* 2020 Multi-compartment 3D-cultured organ-on-a-chip: towards a biomimetic lymph node for drug development. *Pharmaceutics* **12**, 464. (doi:10.3390/pharmaceutics12050464)
30. Tretiakova R, Setukha A, Savinkov R, Grebennikov D, Bocharov G. 2021 Mathematical modeling of lymph node drainage function by neural network. *Mathematics* **9**, 3093. (doi:10.3390/math9233093)
31. Giancesio G, Girelli A, Musesti A. 2021 A model of the pulsatile fluid flow in the lymph node. *Mech. Res. Commun.* **116**, 103743. (doi:10.1016/j.mechrescom.2021.103743)
32. Giancesio G, Girelli A, Musesti A. 2022 A mathematical description of the flow in a spherical lymph node. *Bull. Math. Biol.* **84**, 142. (doi:10.1007/s11538-022-01103-6)
33. Discacciati M, Quarteroni A. 2009 Navier-Stokes/Darcy coupling: modeling, analysis, and numerical approximation. *Rev. Mat. Complut.* **22**, 315–426. (doi:10.5209/rev\_REMA.2009.v22.n2.16263)
34. Waniewski J. 2006 Mathematical modeling of fluid and solute transport in hemodialysis and peritoneal dialysis. *J. Membr. Sci.* **274**, 24–37. (doi:10.1016/j.memsci.2005.11.038)
35. Formaggia L, Quarteroni A, Veneziani A. 2009 *Cardiovascular mathematics: modeling and simulation of the circulatory system*. Milano, Italy: Springer.
36. Penta R, Ambrosi D, Quarteroni A. 2015 Multiscale homogenization for fluid and drug transport in vascularized malignant tissues. *Math. Models Methods Appl. Sci.* **25**, 79–108. (doi:10.1142/S0218202515500037)
37. Mascheroni P, Penta R. 2017 The role of the microvascular network structure on diffusion and consumption of anticancer drugs. *Int. J. Numer. Methods Biomed. Eng.* **33**, e2857. (doi:10.1002/cnm.2857)
38. Shipley RJ, Chapman SJ. 2010 Multiscale modelling of fluid and drug transport in vascular tumours. *Bull. Math. Biol.* **72**, 1464–1491. (doi:10.1007/s11538-010-9504-9)
39. Penta R, Ambrosi D. 2015 The role of the microvascular tortuosity in tumor transport phenomena. *J. Theor. Biol.* **364**, 80–97. (doi:10.1016/j.jtbi.2014.08.007)



40. Abramowitz M, Stegun IA. 1964 *Handbook of mathematical functions with formulas, graphs, and mathematical tables*, vol. 55. Washington, DC: US Government Printing Office.
41. Ohtani O, Ohtani Y. 2008 Structure and function of rat lymph nodes. *Arch. Histol. Cytol.* **71**, 69–76. (doi:10.1679/aohc.71.69)
42. Bertram C, Macaskill C, Davis M, Moore J. 2017 Valve-related modes of pump failure in collecting lymphatics: numerical and experimental investigation. *Biomech. Model. Mechanobiol.* **16**, 1987–2003. (doi:10.1007/s10237-017-0933-3)
43. Ochoa-Tapia JA, Whitaker S. 1995 Momentum transfer at the boundary between a porous medium and a homogeneous fluid I. Theoretical development. *Int. J. Heat Mass Transfer* **38**, 2635–2646. (doi:10.1016/0017-9310(94)00346-W)
44. Ochoa-Tapia JA, Whitaker S. 1995 Momentum transfer at the boundary between a porous medium and a homogeneous fluid II. Comparison with experiment. *Int. J. Heat Mass Transfer* **38**, 2647–2655. (doi:10.1016/0017-9310(94)00347-X)
45. Tan H, Pillai KM. 2009 Finite element implementation of stress-jump and stress-continuity conditions at porous-medium, clear-fluid interface. *Comput. Fluids* **38**, 1118–1131. (doi:10.1016/j.compfluid.2008.11.006)
46. Adair TH, Guyton AC. 1985 Modification of lymph by lymph nodes. III. Effect of increased lymph hydrostatic pressure. *Am. J. Physiol. Heart Circ. Physiol.* **249**, H777–H782. (doi:10.1152/ajpheart.1985.249.4.H777)
47. Adair TH, Moffatt DS, Paulsen AW, Guyton AC. 1982 Quantitation of changes in lymph protein concentration during lymph node transit. *Am. J. Physiol. Heart Circ. Physiol.* **243**, H351–H359. (doi:10.1152/ajpheart.1982.243.3.H351)
48. Adair TH, Guyton AC. 1983 Modification of lymph by lymph nodes. II. Effect of increased lymph node venous blood pressure. *Am. J. Physiol. Heart Circ. Physiol.* **245**, H616–H622. (doi:10.1152/ajpheart.1983.245.4.H616)
49. Stohrer M, Boucher Y, Stangassinger M, Jain RK. 2000 Oncotic pressure in solid tumors is elevated. *Cancer Res.* **60**, 4251–4255.
50. Kozeny J. 1927 Ueber kapillare Leitung des Wassers im Boden. *Sitzungsber Akad. Wiss.* **136**, 271–306.
51. Carman PC. 1997 Fluid flow through granular beds. *Chem. Eng. Res. Des.* **75**, S32–S48. (doi:10.1016/S0263-8762(97)80003-2)
52. Bouta EM, Wood RW, Brown EB, Rahimi H, Ritchlin CT, Schwarz EM. 2014 In vivo quantification of lymph viscosity and pressure in lymphatic vessels and draining lymph nodes of arthritic joints in mice. *J. Physiol.* **592**, 1213–1223. (doi:10.1113/jphysiol.2013.266700)
53. Happel J, Brenner H. 1983 *Low Reynolds number hydrodynamics: with special applications to particulate media*. The Hague, The Netherlands: Martinus Nijhoff Publishers.
54. Al Sariri T, Penta R. 2022 Multi-scale modelling of nanoparticle delivery and heat transport in vascularised tumours. *Math. Med. Biol.: J. IMA* **39**, 332–367. (doi:10.1093/imammb/dqac009)
55. Al Sariri T, Simitev RD, Penta R. 2023 Optimal heat transport induced by magnetic nanoparticle delivery in vascularised tumours. *J. Theor. Biol.* **561**, 111372. (doi:10.1016/j.jtbi.2022.111372)
56. Bertram C, Macaskill C, Moore J. 2019 Inhibition of contraction strength and frequency by wall shear stress in a single-lymphangion model. *J. Biomech. Eng.* **141**, 111006. (doi:10.1115/1.4043724)
57. Girelli A, Giantesio G, Musesti A, Penta R. 2023 Effective governing equations for dual porosity Darcy–Brinkman systems subjected to inhomogeneous body forces and their application to the lymph node. Figshare. (doi:10.6084/m9.figshare.c.6751500)

## A. Explicit solution

In this section, we find an explicit solution to the macroscopic problem given in Section 3. For simplicity, we assume that the multiscale forces  $\mathbf{f}_v^\epsilon$  and  $\mathbf{f}_m^\epsilon$  vanish and that both porous media are isotropic, that is:

$$\bar{\mathbf{K}}_v = \bar{K}_v \mathbb{I}, \quad \bar{\mathbf{K}}_m = \bar{K}_m \mathbb{I},$$

where, from equations (3.15) and (3.14),  $\bar{\mathbf{K}}_v$  and  $\bar{\mathbf{K}}_m$  correspond to  $\langle \mathbf{K}_v + \mathbf{K}_v (\nabla_{\mathbf{y}} \mathbf{g}_v)^{\mathcal{F}} \rangle_{\Omega_v}$  and  $\langle \frac{d^2}{d\mu} \mathbf{W}_m \rangle_{\Omega_m}$ , respectively. We have that  $\bar{K}_v$  and  $\bar{K}_m$  are constants due to the geometry and the hypotheses used, and they are found solving the cell problems (2.25) and (2.30), respectively, using COMSOL Multiphysics, with  $\alpha = 1$ . Our problem is

$$\begin{cases} \Delta p_v = -M_v [p_m - p_v - \bar{p}] & \text{in } \Omega, \\ \Delta p_m = M_m [p_m - p_v - \bar{p}] & \text{in } \Omega, \\ p_v = \bar{p}_v, \quad p_m = \bar{p}_m & \text{on } \partial\Omega, \end{cases} \quad (\text{A1})$$

where  $M_v = \frac{L_p S^{\text{tot}}}{|\Omega_v^{\text{tot}}| \bar{K}_v}$ , and  $M_m = \frac{L_p S^{\text{tot}}}{|\Omega_m^{\text{tot}}| \bar{K}_m}$ .

We consider a spherical domain  $\Omega$ , denoting by  $r$  the radial coordinate,  $\theta$  the polar coordinate, and  $\phi$  the azimuthal angle. Moreover, we assume axisymmetry with respect to the azimuthal angle  $\phi$ . Hence problem (A1) becomes:

$$\begin{cases} \Delta p_v(r, \theta) = -M_v [p_m(r, \theta) - p_v(r, \theta) - \bar{p}] & r < R, \theta \in [0, 2\pi[, \\ \Delta p_m(r, \theta) = M_m [p_m(r, \theta) - p_v(r, \theta) - \bar{p}] & r < R, \theta \in [0, 2\pi[, \\ p_v(R, \theta) = \bar{p}_v(\theta), \quad p_m(R, \theta) = \bar{p}_m(\theta) & \theta \in [0, 2\pi[, \\ \text{non-degeneracy} & r = 0, \theta \in [0, 2\pi[, \end{cases} \quad (\text{A2})$$

where  $R$  is the radius of the spherical domain.

We define the quantity

$$\psi(r, \theta) = p_m(r, \theta) - p_v(r, \theta), \quad (\text{A3})$$

and, taking the difference between the second and the first equation of the system (A2), we obtain the new problem

$$\begin{cases} \Delta \psi(r, \theta) = M [\psi(r, \theta) - \bar{p}] & r < R, \theta \in [0, 2\pi[, \\ \psi(R, \theta) = \bar{p}_m(\theta) - \bar{p}_v(\theta), & \theta \in [0, 2\pi[, \\ \text{non-degeneracy} & r = 0, \theta \in [0, 2\pi[, \end{cases} \quad (\text{A4})$$

where  $M = M_v + M_m$ . Defining

$$\hat{\psi}(r, \theta) = \psi(r, \theta) - \bar{p}, \quad (\text{A5})$$

we can reformulate the first equation of the system (A4) as

$$\Delta \hat{\psi}(r, \theta) = M \hat{\psi}(r, \theta). \quad (\text{A6})$$

In spherical coordinates, we have:

$$\frac{1}{r^2} \frac{\partial}{\partial r} \left( r^2 \frac{\partial \hat{\psi}(r, \theta)}{\partial r} \right) + \frac{1}{r^2} \frac{1}{\sin \theta} \frac{\partial}{\partial \theta} \left( \sin \theta \frac{\partial \hat{\psi}(r, \theta)}{\partial \theta} \right) = M \hat{\psi}(r, \theta),$$

calling  $\zeta = \cos \theta$ , we obtain

$$\frac{1}{r^2} \frac{\partial}{\partial r} \left( r^2 \frac{\partial \hat{\psi}(r, \zeta)}{\partial r} \right) + \frac{1}{r^2} \frac{\partial}{\partial \zeta} \left( (1 - \zeta^2) \frac{\partial \hat{\psi}(r, \zeta)}{\partial \zeta} \right) = M \hat{\psi}(r, \zeta).$$

We search for a solution in the form

$$\hat{\psi}(r, \zeta) = R(r)Z(\zeta);$$

we obtain (multiplying by  $r^2$ , dividing by  $\hat{\psi}$  and rearranging the terms):

$$\frac{1}{R(r)} \frac{\partial}{\partial r} \left( r^2 \frac{\partial R(r)}{\partial r} \right) - r^2 M = -\frac{1}{Z(\zeta)} \frac{\partial}{\partial \zeta} \left( (1 - \zeta^2) \frac{\partial Z(\zeta)}{\partial \zeta} \right), \quad (\text{A7})$$

and we obtain the two differential equations:

$$r^2 \frac{\partial^2 R(r)}{\partial r^2} + 2r \frac{\partial R(r)}{\partial r} - (Mr^2 + n(n+1))R(r) = 0, \quad (\text{A8})$$

$$\frac{\partial}{\partial \zeta} \left( (1 - \zeta^2) \frac{\partial Z(\zeta)}{\partial \zeta} \right) + n(n+1)Z(\zeta) = 0, \quad (\text{A9})$$

where  $n \in \mathbb{N}$ .

The differential equation (A8) is in the form of a spherical Bessel equation, of which the solution is

$$R(r) = Aj_{-n-1}(i\sqrt{Mr}) + By_{-n-1}(i\sqrt{Mr}), \quad (\text{A10})$$

where  $j_{-n-1}$  and  $y_{-n-1}$  are the spherical Bessel function of the first and second kind, respectively, and are connected to the classical Bessel function with the relations:

$$j_{-n-1}(x) = \sqrt{\frac{\pi}{2x}} J_{-n-1+\frac{1}{2}}(x), \quad y_{-n-1}(x) = \sqrt{\frac{\pi}{2x}} Y_{-n-1+\frac{1}{2}}(x), \quad (\text{A11})$$

where  $J_{-n-\frac{1}{2}}$  and  $Y_{-n-\frac{1}{2}}$  are the Bessel function of the first and second kind. The differential equation (A9) is in the form of the Legendre differential equation, of which the solution is

$$Z(\zeta) = CP_n(\zeta) + DQ_n(\zeta), \quad (\text{A12})$$

where  $P_n$  and  $Q_n$  are the Legendre polynomials of the first and second kind, respectively. From the non-degeneracy at  $r = 0$ , we obtain

$$A = D = 0.$$

Using the following property

$$Y_{-n-\frac{1}{2}}(x) = (-1)^n J_{n+\frac{1}{2}}(x),$$

and the fact that

$$J_n(ix) = i^n I_n(x),$$

where  $I_n$  is the modified Bessel function of the first kind of order  $n$ , we have that the solution is

$$\hat{\psi}(r, \zeta) = \sum_{n=0}^{\infty} \tilde{A}_n \frac{1}{\sqrt{r}} I_{n+\frac{1}{2}}(\sqrt{Mr}) P_n(\zeta), \quad (\text{A13})$$

and then, using (A5), we obtain

$$\psi(r, \zeta) = \bar{p} + \sum_{n=0}^{\infty} \tilde{A}_n \frac{1}{\sqrt{r}} I_{n+\frac{1}{2}}(\sqrt{Mr}) P_n(\zeta), \quad (\text{A14})$$

with the boundary condition from the second equation in the system (A4)

$$\psi(R, \zeta) = \bar{p}_m(\zeta) - \bar{p}_v(\zeta). \quad (\text{A15})$$

From the properties of the orthogonal Legendre polynomials [39,52], we can rewrite

$$\bar{p}_m(\zeta) - \bar{p}_v(\zeta) = \sum_{n=0}^{\infty} b^{(n)} P_n(\zeta), \quad (\text{A16})$$

where

$$b^{(n)} = \frac{1}{2}(2n+1) \int_{-1}^1 [\bar{p}_m(\zeta) - \bar{p}_v(\zeta)] P_n(\zeta) d\zeta, \quad (\text{A17})$$

and, recalling that  $P_0(\zeta) = 1$ , we can rewrite equation (A15) as:

$$\begin{aligned} \psi(R, \zeta) - (\bar{p}_m(\zeta) - \bar{p}_v(\zeta)) &= \left[ \bar{p} + \tilde{A}_0 \frac{1}{\sqrt{R}} I_{n+\frac{1}{2}}(\sqrt{MR}) - b^{(0)} \right] P_0(\zeta) \\ &+ \sum_{n=1}^{\infty} \left[ \tilde{A}_n \frac{1}{\sqrt{R}} I_{n+\frac{1}{2}}(\sqrt{MR}) - b^{(n)} \right] P_n(\zeta) = 0, \end{aligned}$$

and using the linear independence of the Legendre polynomials, we obtain, for  $n = 0$ :

$$\tilde{A}_0 = \frac{[b^{(0)} - \bar{p}] \sqrt{R}}{I_{\frac{1}{2}}(\sqrt{MR})}, \quad (\text{A18})$$

and for  $n \in \mathbb{N}$ ,  $n \geq 1$ :

$$\tilde{A}_n = \frac{b^{(n)} \sqrt{R}}{I_{n+\frac{1}{2}}(\sqrt{MR})}. \quad (\text{A19})$$

Exploiting the function  $\psi$  found in equation (A14) with (A18), (A19) and (A5), we can rewrite the first two equations in the system (A2) in this way:

$$\Delta p_m(r, \zeta) = M_m \hat{\psi}(r, \zeta) = M_m \sum_{n=0}^{\infty} \tilde{A}_n \frac{1}{\sqrt{r}} I_{n+\frac{1}{2}}(\sqrt{Mr}) P_n(\zeta) \quad (\text{A20})$$

$$\Delta p_v(r, \zeta) = -M_v \hat{\psi}(r, \zeta) = -M_v \sum_{n=0}^{\infty} \tilde{A}_n \frac{1}{\sqrt{r}} I_{n+\frac{1}{2}}(\sqrt{Mr}) P_n(\zeta). \quad (\text{A21})$$

Now we search the solutions of equations (A20) and (A21) in these forms:

$$p_m(r, \zeta) = \sum_{n=0}^{\infty} m_n(r) P_n(\zeta), \quad (\text{A22})$$

$$p_v(r, \zeta) = \sum_{n=0}^{\infty} v_n(r) P_n(\zeta). \quad (\text{A23})$$

We focus on the equations for  $p_m$  (A20) and (A22), but for the equations in  $p_v$  the computations are similar. Substituting (A22) into the equation (A20), we obtain (in spherical coordinates):

$$\begin{aligned} \sum_{n=0}^{\infty} \left( \frac{1}{r^2} \frac{\partial}{\partial r} \left( r^2 \frac{\partial m_n(r)}{\partial r} \right) \right) P_n(\zeta) + \frac{1}{r^2} \frac{\partial}{\partial \zeta} \left( (1 - \zeta^2) \frac{\partial P_n(\zeta)}{\partial \zeta} \right) m_n(r) \\ - M_m \tilde{A}_n \frac{1}{\sqrt{r}} I_{n+\frac{1}{2}}(\sqrt{Mr}) P_n(\zeta) = 0, \end{aligned}$$

using the fact that  $P_n(\zeta)$  is the Legendre polynomial and the form of the Legendre differential equation (A9), we have

$$\sum_{n=0}^{\infty} \left[ \left( \frac{1}{r^2} \frac{\partial}{\partial r} \left( r^2 \frac{\partial m_n(r)}{\partial r} \right) \right) - \frac{n(n+1)}{r^2} m_n(r) - M_m \tilde{A}_n \frac{1}{\sqrt{r}} I_{n+\frac{1}{2}}(\sqrt{Mr}) \right] P_n(\zeta) = 0,$$

and, from the linear independence of the Legendre polynomials and for every  $n$ , we obtain:

$$m_n''(r) + \frac{2}{r} m_n'(r) - \frac{n(n+1)}{r^2} m_n(r) = M_m \tilde{A}_n r^{\frac{1}{2}} I_{n+\frac{1}{2}}(\sqrt{Mr}). \quad (\text{A24})$$

The homogeneous part of equation (A24) is

$$m_n''(r) + \frac{2}{r} m_n'(r) - \frac{n(n+1)}{r^2} m_n(r) = 0,$$

and the solution is

$$m_n^{(0)}(r) = c_1^{(n)} r^n + c_2^{(n)} r^{-n-1}. \quad (\text{A25})$$

Looking for a particular solution of equation (A24), we compute the Wronskian  $Wr$ :

$$Wr = \frac{-2n-1}{r^2},$$

hence a particular solution is given by

$$m_n^{(p)}(r) = \bar{c}_1^{(n)}(r)y_1(r) + \bar{c}_2^{(n)}(r)y_2(r),$$

where  $y_1$  and  $y_2$  are the independent solutions of the homogeneous equation and

$$\bar{c}_1^{(n)}(r) = - \int \frac{y_2(r)f(r)}{Wr(r)} dr, \quad \bar{c}_2^{(n)}(r) = \int \frac{y_1(r)f(r)}{Wr(r)} dr.$$

We have

$$\bar{c}_1^{(n)}(r) = \frac{M_m \tilde{A}_n}{2n+1} \int r^{-n+\frac{1}{2}} I_{n+\frac{1}{2}}(\sqrt{M}r) dr,$$

calling  $t = \sqrt{M}r$  we obtain

$$\frac{M_m \tilde{A}_n}{2n+1} \int r^{-n+\frac{1}{2}} I_{n+\frac{1}{2}}(\sqrt{M}r) dr = \frac{M_m \tilde{A}_n}{2n+1} \left( \frac{1}{\sqrt{M}} \right)^{-n+\frac{3}{2}} \int t^{-n+\frac{1}{2}} I_{n+\frac{1}{2}}(t) dt, \quad (\text{A26})$$

and using the property

$$\int x^{-p+1} I_p(x) dx = x^{1-p} I_{p-1}(x) dx,$$

we have

$$\frac{M_m \tilde{A}_n}{2n+1} \left( \frac{1}{\sqrt{M}} \right)^{-n+\frac{3}{2}} \int t^{-n+\frac{1}{2}} I_{n+\frac{1}{2}}(t) dt = \frac{M_m \tilde{A}_n}{2n+1} \left( \frac{1}{\sqrt{M}} \right)^{-n+\frac{3}{2}} t^{-n+\frac{1}{2}} I_{n-\frac{1}{2}}(t),$$

and it follows that

$$\bar{c}_1^{(n)}(r) = \frac{M_m \tilde{A}_n}{(2n+1)\sqrt{M}} r^{-n+\frac{1}{2}} I_{n-\frac{1}{2}}(\sqrt{M}r).$$

For  $\bar{c}_2^{(n)}(r)$  we have

$$\bar{c}_2^{(n)}(r) = - \frac{M_m \tilde{A}_n}{2n+1} \int r^{n+\frac{3}{2}} I_{n+\frac{1}{2}}(\sqrt{M}r) dr,$$

calling  $t = \sqrt{M}r$  we obtain

$$- \frac{M_m \tilde{A}_n}{2n+1} \int r^{n+\frac{3}{2}} I_{n+\frac{1}{2}}(\sqrt{M}r) dr = - \frac{M_m \tilde{A}_n}{2n+1} \left( \frac{1}{\sqrt{M}} \right)^{n+\frac{5}{2}} \int t^{n+\frac{3}{2}} I_{n+\frac{1}{2}}(t) dt,$$

and using the following property of the Bessel function

$$\int x^{p+1} I_p(x) dx = x^{p+1} I_{p+1}(x) dx,$$

we have

$$- \frac{M_m \tilde{A}_n}{2n+1} \left( \frac{1}{\sqrt{M}} \right)^{n+\frac{5}{2}} \int t^{n+\frac{3}{2}} I_{n+\frac{1}{2}}(t) dt = - \frac{M_m \tilde{A}_n}{2n+1} \left( \frac{1}{\sqrt{M}} \right)^{n+\frac{5}{2}} t^{n+\frac{3}{2}} I_{n+\frac{3}{2}}(t),$$

and it follows that

$$\bar{c}_2^{(n)}(r) = - \frac{M_m \tilde{A}_n}{(2n+1)\sqrt{M}} r^{n+\frac{3}{2}} I_{n+\frac{3}{2}}(\sqrt{M}r).$$

Finally, the particular solution is

$$m_n^{(p)}(r) = \frac{M_m \tilde{A}_n \sqrt{r}}{(2n+1)\sqrt{M}} \left( I_{n-\frac{1}{2}}(\sqrt{M}r) - I_{n+\frac{3}{2}}(\sqrt{M}r) \right) = \frac{M_m \tilde{A}_n}{M} \frac{1}{\sqrt{r}} I_{n+\frac{1}{2}}(\sqrt{M}r), \quad (\text{A27})$$

where we used the fact that

$$I_{p-1}(x) - I_{p+1}(x) = \frac{2p}{x} I_p(x).$$

Hence we have that the solution is:

$$m_n(r) = m_n^{(0)}(r) + m_n^{(p)}(r) = c_1^{(n)} r^n + c_2^{(n)} r^{-n-1} + \frac{M_m \tilde{A}_n}{M} \frac{1}{\sqrt{r}} I_{n+\frac{1}{2}} \left( \sqrt{M} r \right). \quad (\text{A28})$$

By similar computations we obtain that  $v_n(r)$  in (A23) is

$$v_n(r) = d_1^{(n)} r^n + d_2^{(n)} r^{-n-1} - \frac{M_v \tilde{A}_n}{M} \frac{1}{\sqrt{r}} I_{n+\frac{1}{2}} \left( \sqrt{M} r \right). \quad (\text{A29})$$

We impose the boundary conditions (A2). To have non-degeneracy at  $r = 0$ , for every  $n$  we need that

$$c_2^{(n)} = d_2^{(n)} = 0;$$

on the other hand, rewriting the boundary condition at  $r = R$  in terms of Legendre polynomials

$$\bar{p}_m(R, \zeta) = \sum_{n=0}^{\infty} b_m^{(n)} P_n(\zeta), \quad \bar{p}_v(R, \zeta) = \sum_{n=0}^{\infty} b_v^{(n)} P_n(\zeta),$$

where

$$b_m^{(n)} = \frac{1}{2} (2n+1) \int_{-1}^1 \bar{p}_m(\zeta) P_n(\zeta) d\zeta, \quad b_v^{(n)} = \frac{1}{2} (2n+1) \int_{-1}^1 \bar{p}_v(\zeta) P_n(\zeta) d\zeta,$$

we obtain, using the linear independence of the Legendre polynomials:

$$c_1^{(n)} = \frac{\left[ b_m^{(n)} - \frac{M_m \tilde{A}_n}{M \sqrt{R}} I_{n+\frac{1}{2}} \left( \sqrt{M} R \right) \right]}{R^n}, \quad (\text{A30})$$

$$d_1^{(n)} = \frac{\left[ b_v^{(n)} + \frac{M_v \tilde{A}_n}{M \sqrt{R}} I_{n+\frac{1}{2}} \left( \sqrt{M} R \right) \right]}{R^n}. \quad (\text{A31})$$

## B. Lymph Node Data

The aim of this section is to justify the choices made on the values of the parameters of Table 2.

We assume a radius  $R = 0.49$  mm of the LC [18,23]. The lymph that flows inside the lymph node is modeled as an incompressible Newtonian fluid similar to water [20] with viscosity  $\mu = 1 \frac{\text{mg}}{\text{mm s}}$  and density  $\rho_0 = 1 \frac{\text{mg}}{\text{mm}^3}$ . The interstitial permeability is considered homogeneous [16] with value  $\hat{K}_m = 3.84 \times 10^{-9} \text{ mm}^2$  [29]. The effective viscosity is taken as  $\mu_e = \frac{\mu}{\phi}$  [43,45], where  $\phi$  is the porosity taken as  $\phi = 0.75$  [29].

The parameters that regulate the fluid exchange between the lymph node and the blood vessels are very heterogeneous in the literature, but we try to summarize them here. The Staverman's reflection coefficient  $\sigma$  is estimated between  $\sigma = 0.88 - 0.9$ . In [41,46,47] they estimate the oncotic pressure difference  $\pi_v - \pi_m$  in a canine popliteal lymph node as  $\approx 2080$  Pa =  $2.08 \times 10^6$  mPa, in [22] they estimate the values  $\pi_v \approx 1.53 \times 10^6$  mPa and  $\pi_m \approx 5.06 \times 10^6$  mPa in a mouse using the assumption that the protein content of lymph is 40% of that of the plasma, [27,28] found  $\pi_v - \pi_m \approx 3.41 \times 10^5$  mPa by fitting the wild type mouse model to experimental data, [48] measured the value  $\pi_v - \pi_m \approx 1.5 \times 10^6$  mPa in the skin of mice and [30] estimates  $\pi_v - \pi_m \approx 1.69 \times 10^6$  mPa.

For the hydraulic conductivity of the blood vessel wall  $L_p$ , we have that [22] assumed a value of  $L_p = 5.475 \times 10^{-12} \frac{\text{mm}}{\text{s mPa}}$  based on the measured hydraulic conductivity of rat mesenteric venular microvessels, [27,28] assumed a range of  $L_p \approx 1.02 \times 10^{-11} - 6.7 \times 10^{-10} \frac{\text{mm}}{\text{s mPa}}$  from the values of the blood capillaries, [30] estimates directly  $L_p \frac{S^{\text{tot}}}{|\Omega^{\text{tot}}|} \approx 10^{-6} \frac{1}{\text{s mPa}}$  (that means, in our case,  $L_p \approx 3.667 \times 10^{-8} \frac{\text{mm}}{\text{s mPa}}$ , see below).

Moreover, we have that the mean blood vessels pressure  $\bar{p}_v$  in the node is estimated as  $\bar{p}_v \approx 6.67 \times 10^5$  mPa in [22], as  $\bar{p}_v \approx 9.73 \times 10^5$  mPa in [27,28] and as  $\bar{p}_v \approx 1.06 \times 10^6$  mPa in [30].

The surface of fluid exchange  $S^{\text{tot}}$  between the lymph node and the blood vessels is given by an average of the values found in [23] and it is

$$S^{\text{tot}} = 13.4 \text{ mm}^2; \quad (\text{B1})$$

the volume of the blood vessels inside the node  $|\Omega_v^{\text{tot}}|$  is about the 6.15% of the whole lymph node volume [23,24], and hence we have (supposing that the SCS height is  $\approx 10^{-2}$  mm [18,22,32])

$$|\Omega_v^{\text{tot}}| = 0.0322 \text{ mm}^3. \quad (\text{B2})$$

We suppose the geometry of the cell domain is as in Figure 1. This microscale geometry is simpler with respect to the physiological one [23,24]; we can assume this simplified microscale geometry because we start with a formulation that is already smoothed out (our starting point was a Darcy/Darcy-Brinkman formulation). Hence, we do not need precise information about the microstructure geometry. What we want to keep in the physiological geometry are the surface area of the blood vessels  $S^{\text{tot}}$  and the volume of the blood vessels  $|\Omega_v^{\text{tot}}|$ . For this reason, we estimate the normalized radius of the cylinders  $\hat{r}_c = r_c/d$ , where  $r_c$  is the radius of the cylinders and  $d$  is the microscale variable that indicates the distance between the centers of the cylinders, in such a way that we keep the physiological parameters  $S^{\text{tot}}$  and  $|\Omega_v^{\text{tot}}|$ . For a spherical lymph node as in our case, the total volume is

$$|\Omega| = 0.5236 \text{ mm}^3. \quad (\text{B3})$$

It follows that

$$|\Omega_m^{\text{tot}}| = 0.4914 \text{ mm}^3. \quad (\text{B4})$$

From these values, we have that

$$|\Omega_m| = \frac{|\Omega_m^{\text{tot}}|}{|\Omega|} = \frac{0.4914 \text{ mm}^3}{0.5236 \text{ mm}^3} = 0.9385, \quad (\text{B5})$$

$$|\Omega_v| = \frac{|\Omega_v^{\text{tot}}|}{|\Omega|} = \frac{0.0322 \text{ mm}^3}{0.5236 \text{ mm}^3} = 0.06149, \quad (\text{B6})$$

and hence we have

$$|\Omega_m| + |\Omega_v| = 1. \quad (\text{B7})$$

We have that the cell volume is  $d^3$ , and hence for  $N$  cells we have

$$Nd^3 = |\Omega|. \quad (\text{B8})$$

The radius of the normalized cylinders that gives us the volume fraction values  $|\Omega_m|$  and  $|\Omega_v|$  is found numerically using COMSOL Multiphysics, and it is

$$\hat{r}_c = \frac{r_c}{d} = 0.0869, \quad (\text{B9})$$

and it follows that

$$r_c = 0.0869d. \quad (\text{B10})$$

We have that the surface area of the tricylinder of our cell problem is

$$3 \left[ 2\pi r_c d - (16 - 8\sqrt{2})r_c^2 \right], \quad (\text{B11})$$

and for  $N$  cells, we have that the total surface of the blood vessel network is

$$3N \left[ 2\pi r_c d - (16 - 8\sqrt{2})r_c^2 \right]; \quad (\text{B12})$$

using the relation (B10), equation (B12) becomes

$$3N \left[ 2\pi \frac{r_c^2}{0.0869} - (16 - 8\sqrt{2})r_c^2 \right]. \quad (\text{B13})$$

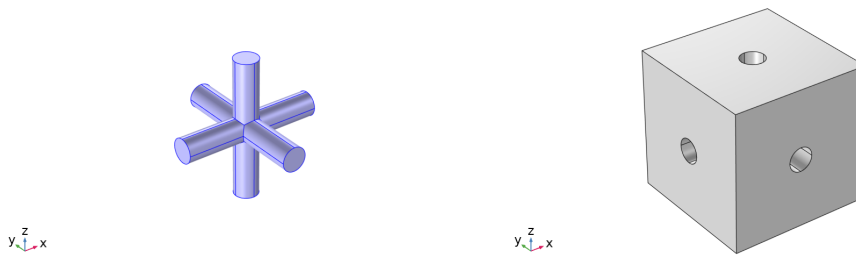


**Figure 1.** The cell problem domains  $\Omega_v$  (left) and  $\Omega_m$  (right) in a non-dimensional form. The cube has side 1 and the tricylinder has radius  $\bar{r} = r_c/d$ .

Imposing that the total surface of the tricylinders (B13) equal to the blood network surface area  $S^{\text{tot}}$  (B1), we obtain

$$Nr_c^2 = 0.1981. \quad (\text{B14})$$

Putting together equations (B8), (B10) and (B14), we obtain a system with three equations and three unknowns:

$$\begin{cases} Nd^3 = |\Omega|, \\ r_c = 0.0869d, \\ Nr_c^2 = 0.1981; \end{cases} \quad (\text{B15})$$

solving this system gives us the values  $d \approx 0.02$  mm,  $r_c \approx 0.0017$  mm and  $N \approx 1310$ . Thanks to this estimation, we have that, at the macroscale,  $S^{\text{tot}}$  and  $|\Omega_v^{\text{tot}}|$  are the same as in the physiological data. Hence we can use these parameters to estimate the hydraulic conductivity of the blood vessels  $K_v$  using the Kozeny-Carman formula [49,50]:

$$K_v = \frac{1}{c_0 \left( \frac{S}{|\Omega_v|} \right)^2}, \quad (\text{B16})$$

where  $c_0$  is the *Kozeny constant* and depends on the tortuosity of the vessels [38]. In the case with little tortuosity, we can take into account the tortuosity effect by varying only the constant  $c_0$  and not the geometry of the cell problem. However, to study the role of tortuosity in more detail, we need to take it into account in the geometry of the microscale problem, which we did not do in this case. With no tortuosity effect,  $c_0 = 5.6$ , and this implies  $K_v = 1.03 \times 10^{-6} \text{ mm}^2$ .

Moreover, with these data, we have

$$\epsilon = \frac{d}{L} \approx 10^{-2}.$$

## C. Numerical Simulations

In this section we discuss the numerical simulations used to find the solutions of the cell problems (2.25), (2.26), (2.30) and (2.31). We can see the geometry of the cell problems using the data found in Appendix B in Figure 1. For the sake of simplicity, we assume that the multiscale forces  $\mathbf{f}_v^\epsilon$  and  $\mathbf{f}_m^\epsilon$  vanish; hence the unique solutions of the cell problems (2.26) and (2.31) are zero (remembering that  $\langle \tilde{g}_m(\mathbf{x}, \mathbf{y}) \rangle_{\Omega_m} = 0$  and  $\langle \tilde{g}_v(\mathbf{x}, \mathbf{y}) \rangle_{\Omega_v} = 0$ ). Moreover, we assume that both porous media are isotropic, which means that the solutions of the cell problems (2.25) and (2.30) are in these forms

$$\mathbf{W}_m = W_m \mathbb{I}, \quad \nabla_{\mathbf{x}} g_v = G_v \mathbb{I},$$

where  $W_m$  and  $G_v$  are constants due to the geometry symmetry of the cell problems and the hypotheses used.



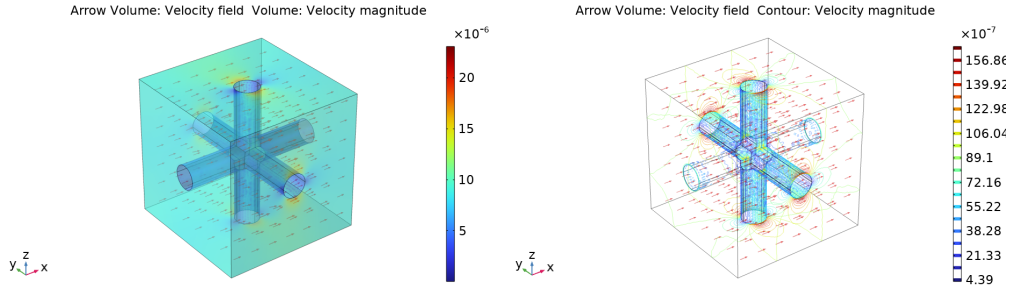


**Figure 2.** The velocity solution of cell problem (2.30) in the geometry  $\Omega_m$  in a non-dimensional form using the physiological data found in Appendix B.

We solve these cell problems using COMSOL Multiphysics, with  $\alpha = 1$ . For the cell problem (2.30) in the geometry  $\Omega_m$ , we use the Brinkman equations module of COMSOL, with a  $\mathbb{P}_2^3 - \mathbb{P}_1$  discretization for the fluid and the pressure variable, respectively; moreover, we use the PARDISO solver. We can see the solution (the velocity) in Figure 2. This solution is calculated in the direction  $e_1$ , but thanks to the geometry symmetry and the isotropy of the porous medium, we have the same solution for every direction.

To find the hydraulic conductivity in (3.1) we need to calculate  $\langle W_m \rangle_{\Omega_m}$ , which is the average of the velocity calculated above, and the value is

$$\langle W_m \rangle_{\Omega_m} \approx 9.1163 \times 10^{-6}. \quad (\text{C1})$$

To study in more detail the mesh of the previous solution, we perform an adaptive mesh refinement study. After this process, we find a value of

$$\langle W_m^{\text{ref}} \rangle_{\Omega_m} \approx 9.1187 \times 10^{-6}, \quad (\text{C2})$$

giving a relative error of  $\approx 0.026\%$ .

The cell problem (2.25) in the geometry  $\Omega_v$  is in the form of Poisson's equation. We use Poisson's equation module in COMSOL with a quadratic element order for the discretization, and we use MUMPS as a solver. We can see the solution in Figure 3. The solution is calculated in the direction  $e_1$  but, as in the previous case, we have the same solution for every direction thanks to the symmetry of the geometry and the isotropy of the porous medium.

We need to calculate  $\langle G_v \rangle_{\Omega_v}$  to find the hydraulic conductivity in (3.4), which is the average of the gradient of the solution calculated above, and the value is

$$\langle G_v \rangle_{\Omega_v} \approx -0.60060. \quad (\text{C3})$$

We perform an adaptive mesh refinement study for this problem as in the previous one. After this process, we find a value of

$$\langle G_v^{\text{ref}} \rangle_{\Omega_m} \approx -0.60054, \quad (\text{C4})$$

giving a relative error of  $\approx 0.01\%$ .

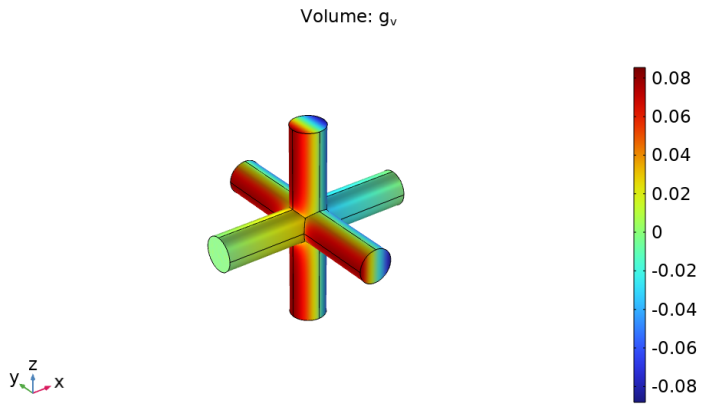


**Figure 3.** The solution of cell problem (2.25) in the geometry  $\Omega_v$  in a non-dimensional form using the physiological data found in Appendix B.